CHAPTER II

EXPERIMENTAL TECHNIQUE AND APPARATUS

High Resolution Infrared Spectroscopy

Throughout the course of this Ph.D. work the infrared absorption spectra of a wide range of van der Waals complexes have been studied. Results from ArDCl[1], NeDCl[1], $(DCl)_2$[2,3], HCl-DCl[4], DCl-HCl[4], and $(HCl)_2$[2,5] are presented in this thesis. All studies reported herein probe either the HCl or DCl vibration within the complex. As the HCl and DCl vibrational frequencies are substantially different (2885.97 cm^{-1} and 2091.06 cm^{-1}, respectively), different infrared spectrometers are used to probe the two chromophores. The HCl vibrations (3.46 μm) are investigated with a difference frequency laser spectrometer (tunable from 2.2 - 4.2 μm), and the DCl vibrations (4.78 μm) with a Pb-salt diode laser (tunable from 4 - 10 μm). These studies are not limited to the lowest energy level in each vibrational state, since low frequency vibrations can be probed via combination, hot, or difference bands (see Figure 1.1). One drawback to studying low frequency vibrations in this manner is that these bands are typically an order of magnitude weaker

than the high frequency intramolecular fundamental vibrations. This is because these vibrations are only infrared active by virtue of a nonzero anharmonicity, as discussed in Chapter I. As will be seen in numerous examples in this text, however, these spectrometers possess the requisite sensitivity for such observations.

We shall spend some time discussing both of these spectrometers. The first section deals with the Pb-salt diode spectrometer, which was constructed as part of this dissertation. This is followed by a shorter discussion of the difference frequency spectrometer, an apparatus which has been discussed previously in detail[6-8]. A short discussion follows regarding the operating principles of the slit pulsed valve and gas handling setup. The chapter concludes with a discussion of the technique used to obtain infrared line shapes.

Infrared Spectrometers

Diode Laser Spectrometer

Operating Principles

A Pb-salt diode laser is one of the most general sources of tunable radiation in near to mid-IR regions. This section will discuss, in some detail, the operating principles of a Pb-salt diode laser[9], and the resulting

slit jet mid-IR spectrometer (shown in Figure 2.1) which we developed within our laboratory. This spectrometer is based around a Laser Photonics SP5800-2 laser source assembly. Briefly, these lasers are composed of a p-n junction which is forward biased. The injected electrons combine with holes and radiate photons with energies determined by the semiconductor band gap, about 2100 cm^{-1} for the studies presented herein.

The gain medium for a Pb-salt diode laser is formed at a p-n junction in semiconductor materials. The p-type layer is characterized by an electron deficiency such that the primary charge carriers are electron holes. The n-type layer, on the other hand, contains excess electrons which serve as the charge carriers. When these layers are placed in contact, electrons and holes in the area of the junction will combine. This will occur until a self induced electric field across the p-n junction balances the charge separation of the electrons and holes. At this point no further recombination occurs (see Figure 2.2).

When an external bias is applied across the junction, electrons are reintroduced to the n-type layer and removed from the p-type layer causing electrons to once again recombine with holes. This recombination results in either a radiative (see Figure 2.3) or nonradiative release of energy. The radiative process is

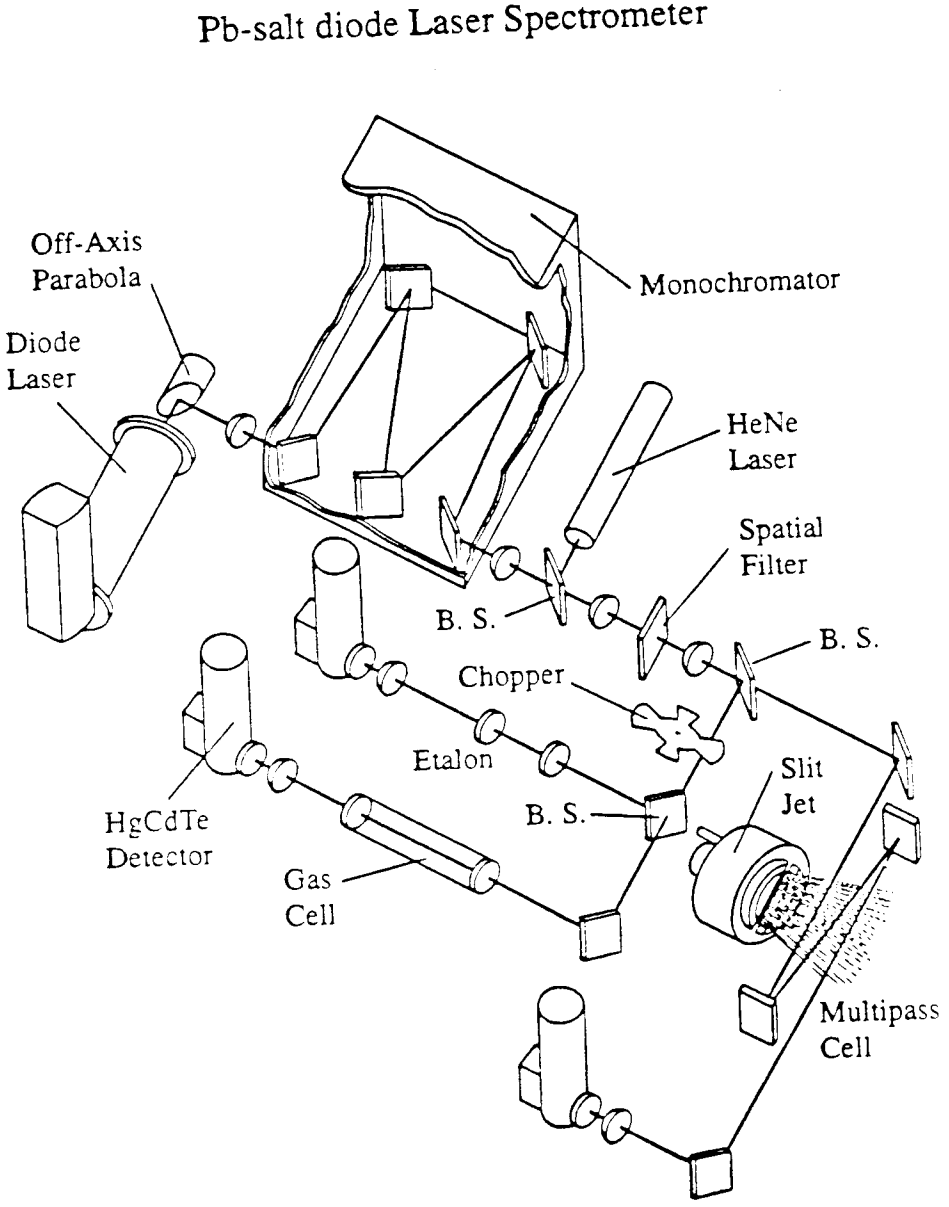

Figure 2.1 Schematic representation of the experimental Pb-salt diode laser spectrometer. The monochromator pictured is not required for these studies due to the near single longitudinal mode characteristics of the diode used. Each beam splitter (B.S.) pictured is a pellicle splitter which reflects approximately 10% of the beam and transmits the remainder. The multipass used for these studies involves six passes through the slit expansion and not three as is schematically shown in this figure.

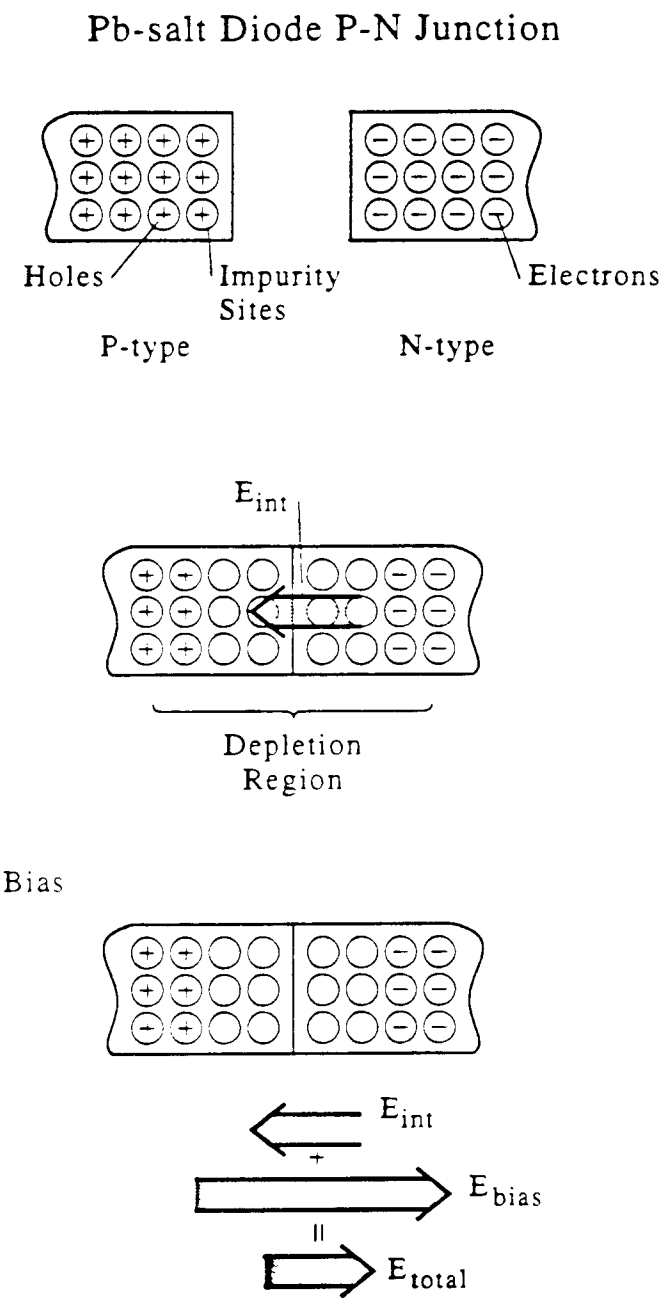

Figure 2.2 Schematic representation of a p-n junction. The top cartoon, pictures perfect p-type and n-type materials, where electrons are the major charge carrier in an n-type material and holes in a p-type. When these materials are placed in contact, the electrons and holes in vicinity of interface will recombine until the internal electric field counters exactly the charge separation. When the junction is forward biased, electrons and holes can once again recombine.

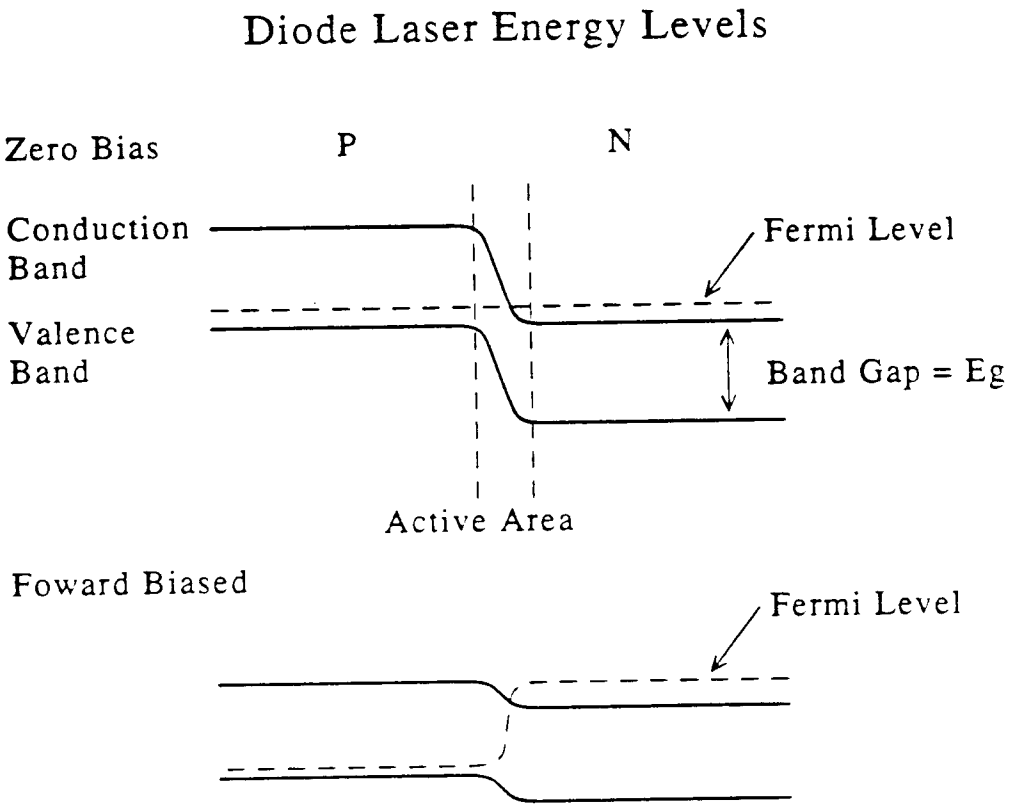

Figure 2.3 An approximate picture of the energy levels of a diode laser. As the diode is forward biased, electrons are injected into the n-type material which can recombine in the region of the interface with holes in the p-type material. The recombination releases energy either radiatively or nonradiatively. The radiative recombination results in photons of energy given by the band gap.

responsible for the lasing of these diodes. The photon energy is determined by the band gap or energy difference between the conduction and valence levels. This band gap is very dependent on the choice of semiconductor material, as well as diode temperature and bias current. Infrared tunable diode lasers are typically composed of Pb-salts, such as $Pb_{1-x}Sn_xTe$ and $PbS_{1-x}Eu_xSe_yTe_{1-y}$. By varying x and y in these semiconductor materials, the band gaps can be adjusted from about 4 to 30 μm. Other Pb-salts are also available which extend this tuning range slightly in each direction. The diode used for all the DCl studies discussed herein was purchased from Laser Photonics (model number SP5615), and has a composition of $Pb_{0.9915}Eu_{0.0085}Se_{0.9905}Te_{0.0055}$. The dimensions of the active region of this diode are 1 μm X 22 μm X 250 μm. The output frequency is centered around 2090 cm^{-1}, with a tuning rate of 1150 MHz/mA.

Lasing is not possible without feedback, which is provided by forming a cavity around the semiconductor material by cleaving the facets. At applied currents less than a threshold value, the photons are emitted incoherently. As the forward bias current is increased, a threshold condition is reached in which the round trip cavity gain exactly equals the losses:

$$\Gamma_{thr} = \alpha_{int} + \alpha_m \qquad (2.1)$$

Here, Γ_{thr} is the gain at threshold, α_{int} represents the internal losses and α_m the transmission losses at the facets. The internal losses include those due to absorption of light in both the active and cladding region and scattering at each heterogeneous interface. Attempts are made to minimize these internal losses. One of the approaches utilized by Laser Photonics is fabrication of the diode in a Mesa Stripe geometry (see Figure 2.4). This design places an active region between two cladding layers, each of which have a higher index of refraction and larger band gap than the active region. These tend to localize the photons and electrons, respectively, in a smaller active region, thus reducing absorption.

The transmission loss (α_m) at the cleaved ends is due to finite output coupling, which is a function of both the cavity length (ℓ) and the reflectance of the facet ends ($R_1 = R_2$).

$$\alpha_m = \frac{1}{2\ell} \ln\left(\frac{1}{R_1 R_2}\right) \qquad (2.2)$$

The diode used for these studies is approximately 250 μm long with a refractive index of 4-6. Thus, the reflectance at the cleaved ends is about 0.71, i.e. a loss of about 14 per cm.

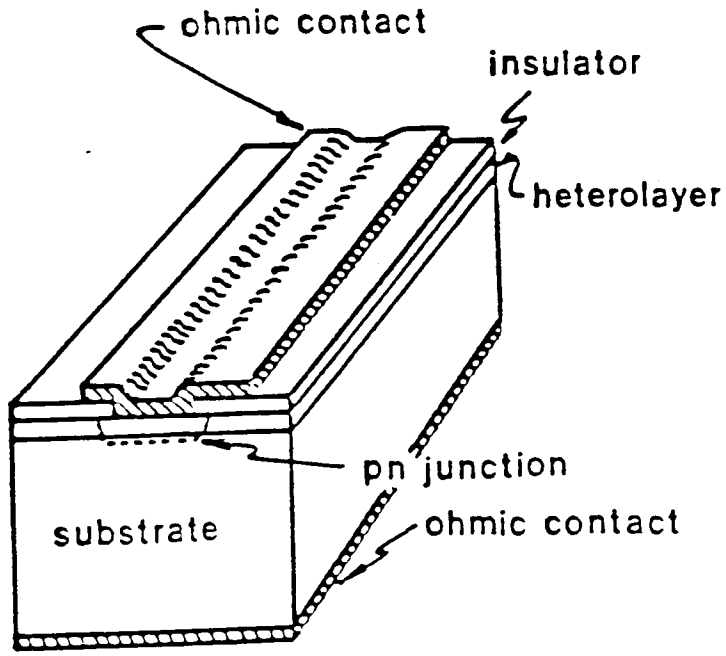

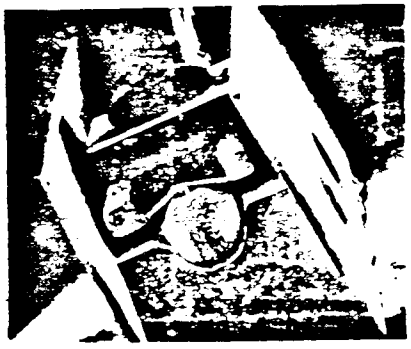

Figure 2.4 A schematic diagram of a mesa stripe construction of diode laser. The active layer is placed between two layers with higher index of refraction and band gap to localize the electrons and photons in the active region. The picture on the bottom half of the figure is that of an actual Pb-salt diode laser.

Both of these loss channels increase with temperature, thus the gain (and therefore the threshold current) needed to overcome these losses increases with increasing temperature. This effect is demonstrated in Figure 2.5, which shows the threshold current versus temperature for the diode used in these studies. At temperatures above about 100 K, the loss channels are so great that lasing is impossible for this diode.

Consequently, one needs to operate at very low temperatures, which are achieved with a commercial closed cycle He refrigerator. This cooling system operates on the principle of adiabatic cooling which accompanies expansion of a gas through a small orifice. The gas is compressed and forced through the orifice by pistons which run at 3 Hz. As will be discussed below, it is this mechanical vibration which is primarily responsible for the laser frequency noise. The cold head assembly, shown in Figure 2.6, is capable of cooling four laser diodes to approximately 15 K.

The output frequency of the diode laser is tuned by adjusting the diode temperature and current. The Pb-salt diode band gap changes with temperature, as much as 200 cm^{-1} for 100 K temperature change. Additionally, the frequency of the lasing mode acquires temperature dependence via a temperature dependent index of refraction.

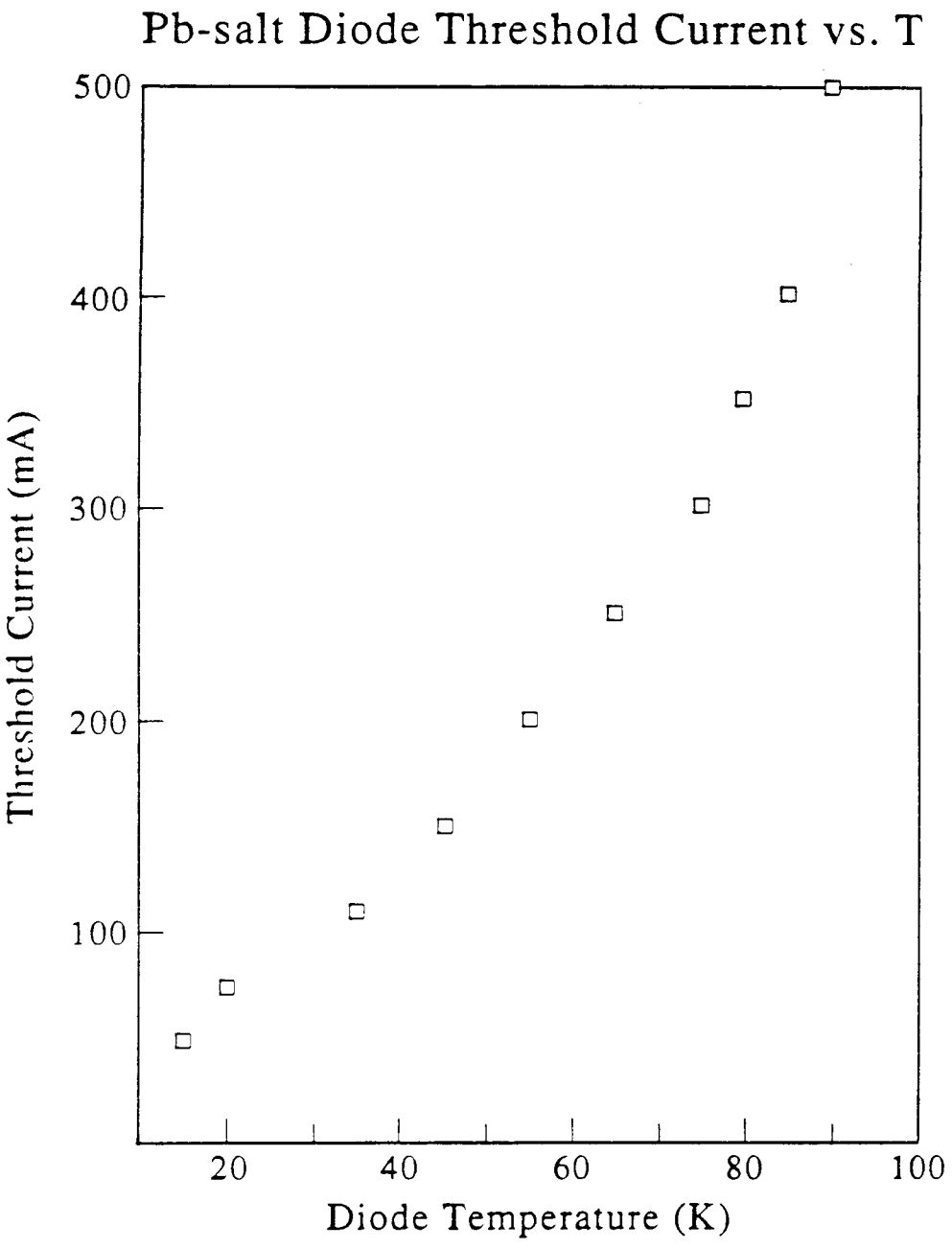

Figure 2.5 A plot of the threshold current versus temperature for the diode used in these studies. The trend of higher threshold current for higher temperature is quite obvious from this plot. The increase in threshold current is due to increasing losses in the cavity with temperature. In fact, this diode, which has an upper current limit of 1 A, will not lase above about 125 K.

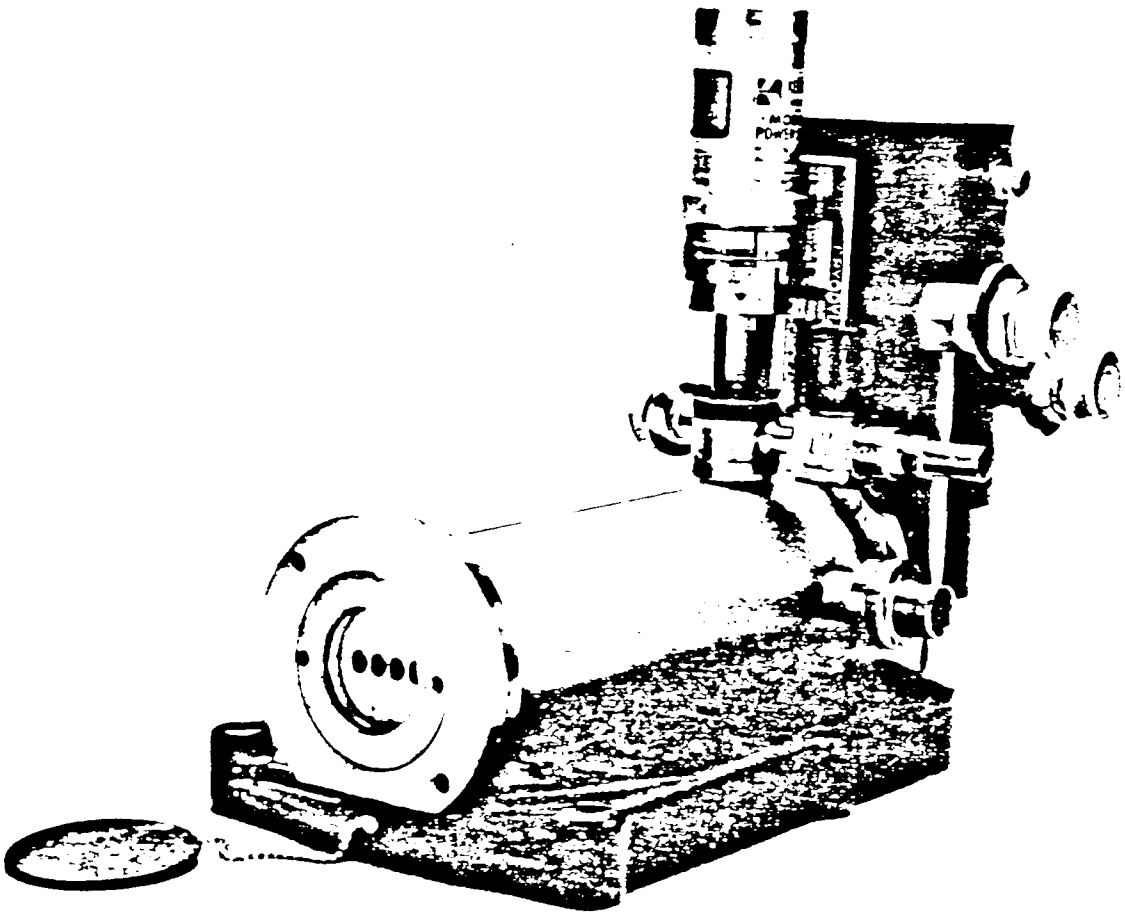

Figure 2.6 A picture of the cold head assembly of the Pb-salt diode laser. The four horizontal holes in the front are the locations of the four diodes which can be mounted at one time. The small cylindrical tube which protrudes vertically up from the cold head is a Modion ion pump. This pump extends the time necessary between warming the diodes to room temperature. This is a desirable addition to the laser since repeated cycling to room temperature degrades the diode characteristics.

$$\nu_m = \frac{mc}{2\mu_m \ell} \qquad (2.3)$$

Where m refers to the mth longitudinal mode, c is the speed of light, μ_m the index of refraction, and ℓ is the cavity length. The diode temperature is controlled both by external heating of the diode and Joule heating due to the current flowing through the diode. As can be seen in Figure 2.7, the spectral modes scan with current in a fairly well defined manner. Figure 2.8 shows a plot of lasing frequency of the diode used in these studies, as a function of both the diode temperature and current. Instead of a single continuous scan, typically scans of no more than about 1-2 cm^{-1} in length are possible. This is because the underlying gain curve does not scan at the same rate with temperature as does the band gap. Also the gain curve is broad enough (10-20 cm^{-1}) to support more than one longitudinal cavity mode. The frequency of these spectral modes can be predicted from Eq. 2.3 knowing the index of refraction and length of the cavity. The spacing between longitudinal modes is simply $\nu_m - \nu_l$, complicated only by the fact that the index of refraction of the diode is frequency dependent (dispersive). Thus, including this dependence, the spacing between adjacent modes becomes.

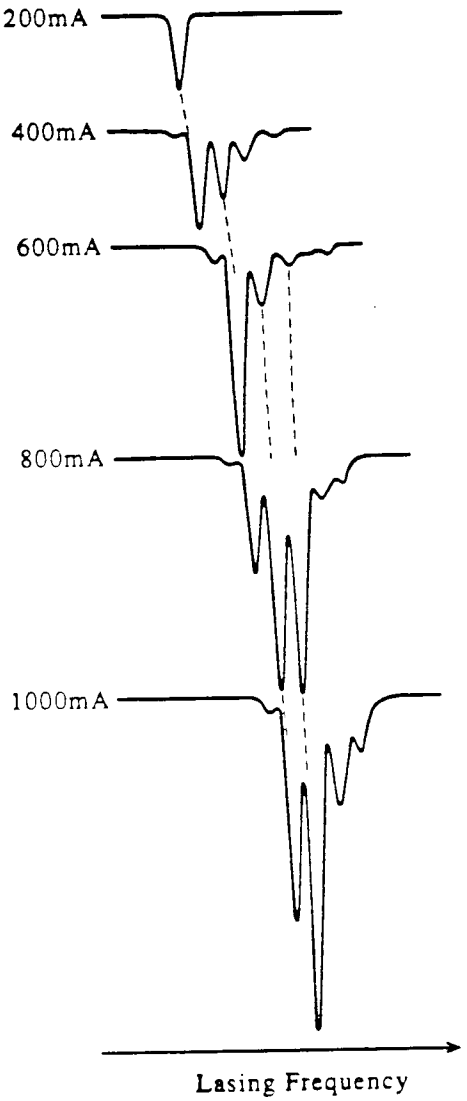

Figure 2.7 A sample set of longitudinal modes for one of the diode lasers which we checked out (not the diode with which these studies were carried out). As for all of the diode lasers we investigated, the laser operates on more than one longitudinal mode. Additionally, the laser frequency scans to higher frequency with increasing current. It is also worth noting that any particular cavity mode grows in intensity and then shrinks. This is due to the differential scanning rates of the cavity modes and the underlying gain curve. Also note that at low current (200 mA for this diode) the laser only emits a single longitudinal mode. This is a general trend for nearly all diodes investigated.

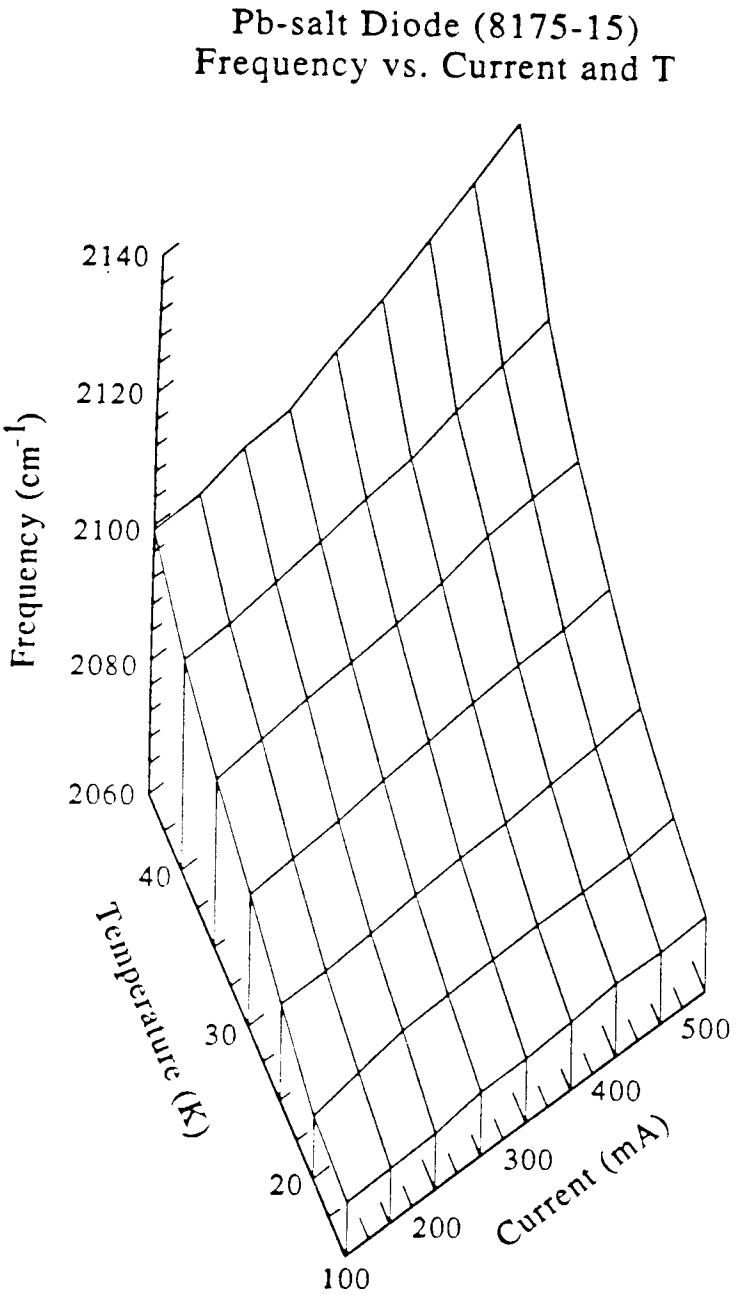

Figure 2.8 Laser frequency versus both temperature and current. All spectra reported in this thesis were taken between 2060 - 2120 cm^{-1} which is in the heart of the scanning region for this diode. The frequency depends more sensitively on temperature than current, and thus one typically locates a frequency region by adjusting the temperature, and then fix the temperature and adjust slowly the current for high resolution scans.

$$\nu_n - \nu_m = \Delta\nu = \frac{c}{2\ell}\left[\frac{n}{\mu_n} - \frac{m}{\mu_m}\right] \qquad (2.4)$$

If the change in index of refraction is negligible between two adjacent longitudinal modes (as is the case for nearly all practical diode dimensions), the separation between two longitudinal modes is simply $c/2\ell\mu$ or 3.3 cm^{-1} for the diode used herein which is very consistent with the 3.0 cm^{-1} separation measured for this diode. However, the index of refraction does vary significantly over the temperature range of the diode, and thus the longitudinal mode spacing changes with diode temperature. This mode structure is not always easily predictable, as can be seen in Figure 2.9. The figure presents two temperature regions of the same diode. At T=105 K, only one longitudinal mode is present, but only 20° lower (T=85 K) at least 13 different longitudinal modes are supporting gain.

While one can typically eliminate all but one of the longitudinal modes with a monochromator, a more favorable solution is for the diode to lase in a single spectral mode. Newer diodes being produced with such techniques as molecular beam epitaxial growth show promise for single mode operation. The diode used for these studies demonstrates remarkably good mode characteristics, eg.

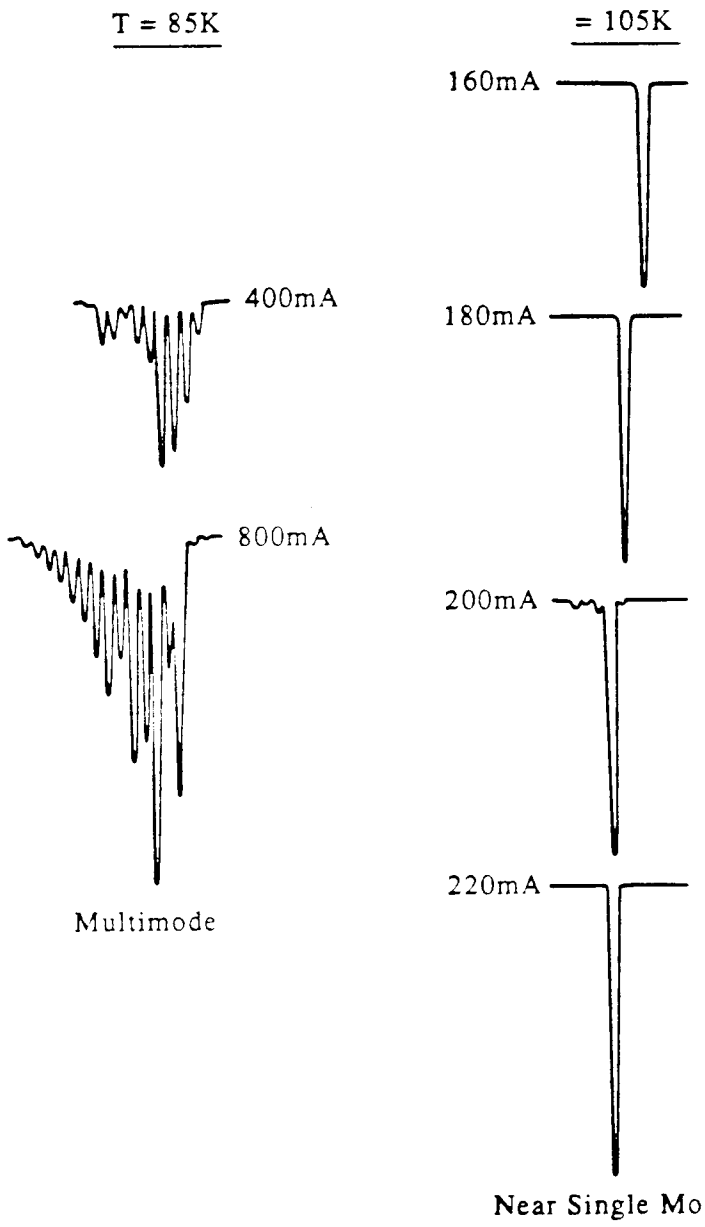

Figure 2.9 A demonstration of very reasonable and unusable mode characteristics, both on the same diode and only 20 K separated in temperature. The higher temperature characteristics are very favorable since only a single longitudinal mode is present. However, the multimode region is unusable since about 6 of more spectral modes have nearly equal intensities, resulting in observation of transitions from each with no a priori manner of determining from which mode an absorption arose.

close to 80-90% of the output power lies in one spectral mode. Absorption peaks due to the remaining <20% of the power are rarely observed, and provide only a minor inconvenience in data analysis. One such observation of secondary mode absorption is shown in Figure 2.10 where two spectral scans through the same region of the NeDCl spectrum are plotted. The large peak in each scan is a DCl monomer transition due to near 100% absorption of the weak secondary mode present in the laser beam. As can be seen by comparing the relative transition frequencies of the NeDCl absorptions (due to the primary mode), and the monomer transitions (due to the secondary mode), the frequency difference between the two longitudinal modes changes with temperature, as discussed above. Thus by scanning over all spectral regions at two different temperatures, one can discriminate between absorptions due to the primary and secondary modes.

In addition to multiple longitudinal modes, Pb-salt diode laser radiation is often composed of multiple spatial modes. These are due to lasing which occurs in separate "filaments" within the active region, thus these modes are referred to as filamentary modes. The presence of these extra modes produces an astigmatic beam, i.e. it is impossible to focus both horizontal and vertical components of the beam simultaneously. The beam is therefore susceptible to overfilling an optic in one

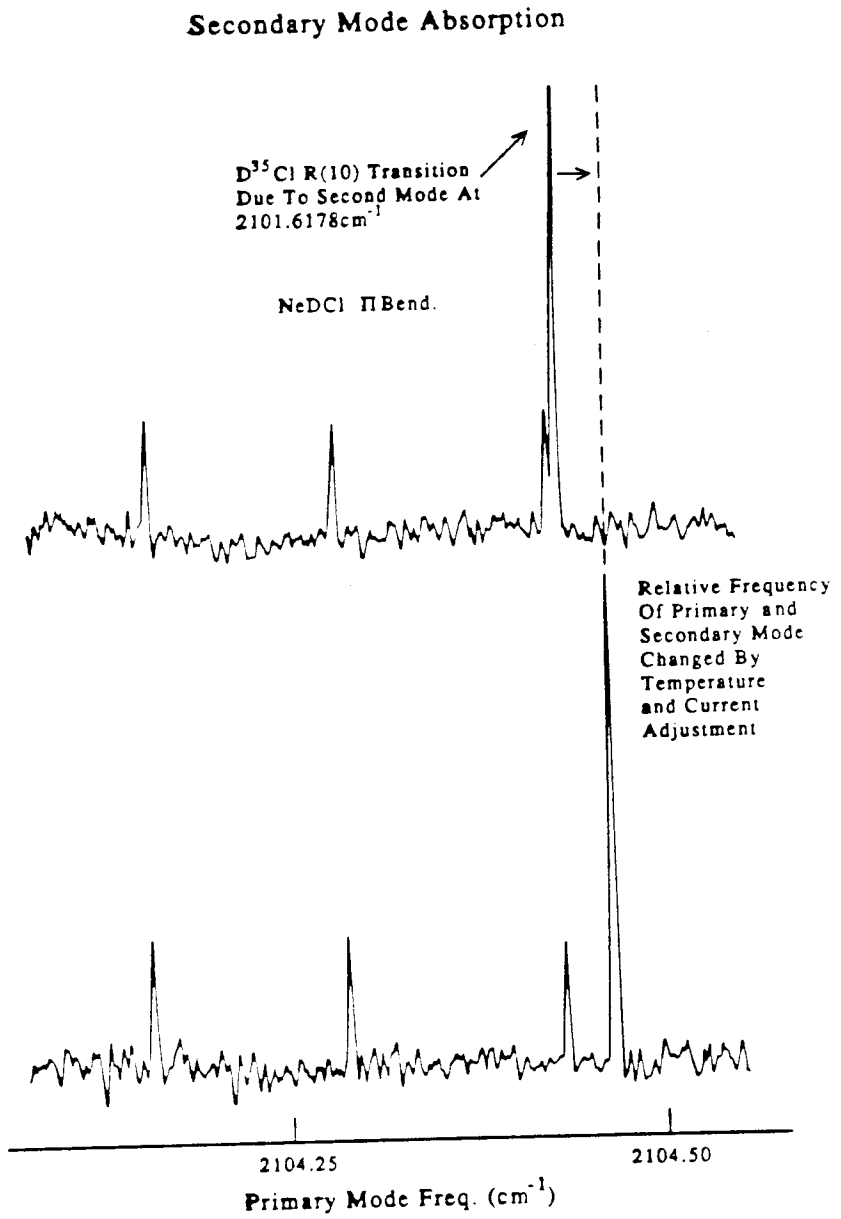

Figure 2.10 The observation of a transition from a secondary mode. This mode is present at less than 10% the power of the primary mode. The transition is only observable since the monomer R(1) transition absorbs essentially all the light in that secondary mode, located about 3 cm^{-1} to lower frequency than the primary mode. Such an observation rarely occurs and can be discriminated by scanning over the same spectral region more than once with different current and temperature. The relative separation between the primary and secondary modes is changed in this manner.

direction. This problem is dealt with very simply by passing the beam through a spatial filter and eliminating all but one spatial mode. We have used a 100 μm hole in Cu foil for this purpose. The beam is focused into the spatial filter with an f/2, 1" diameter CaF_2 plano-convex lens. Routinely, about 50% of the IR radiation is transmitted through the spatial filter. The beam emitted from the spatial filter is recollimated with a f/6, 1" diameter CaF_2 plano-convex lens.

Frequency Noise

In addition to the frequency scanning, output power and spectral mode characteristics discussed above, the magnitude of both amplitude and frequency noise are extremely important criteria to assess the usefulness of this laser for tunable IR spectroscopy. We will delay a discussion of the diode laser amplitude noise until the data acquisition section.

The main source of frequency noise on the diode laser is due to mechanical vibrations which accompany each extension of the piston used to cool the cold head. This is shown unambiguously in Figure 2.11, which is a trace of the laser frequency noise versus time. The plot was obtained by triggering a storage oscilloscope with a microphone positioned near the cold head. The frequency noise is mapped into amplitude noise by positioning the

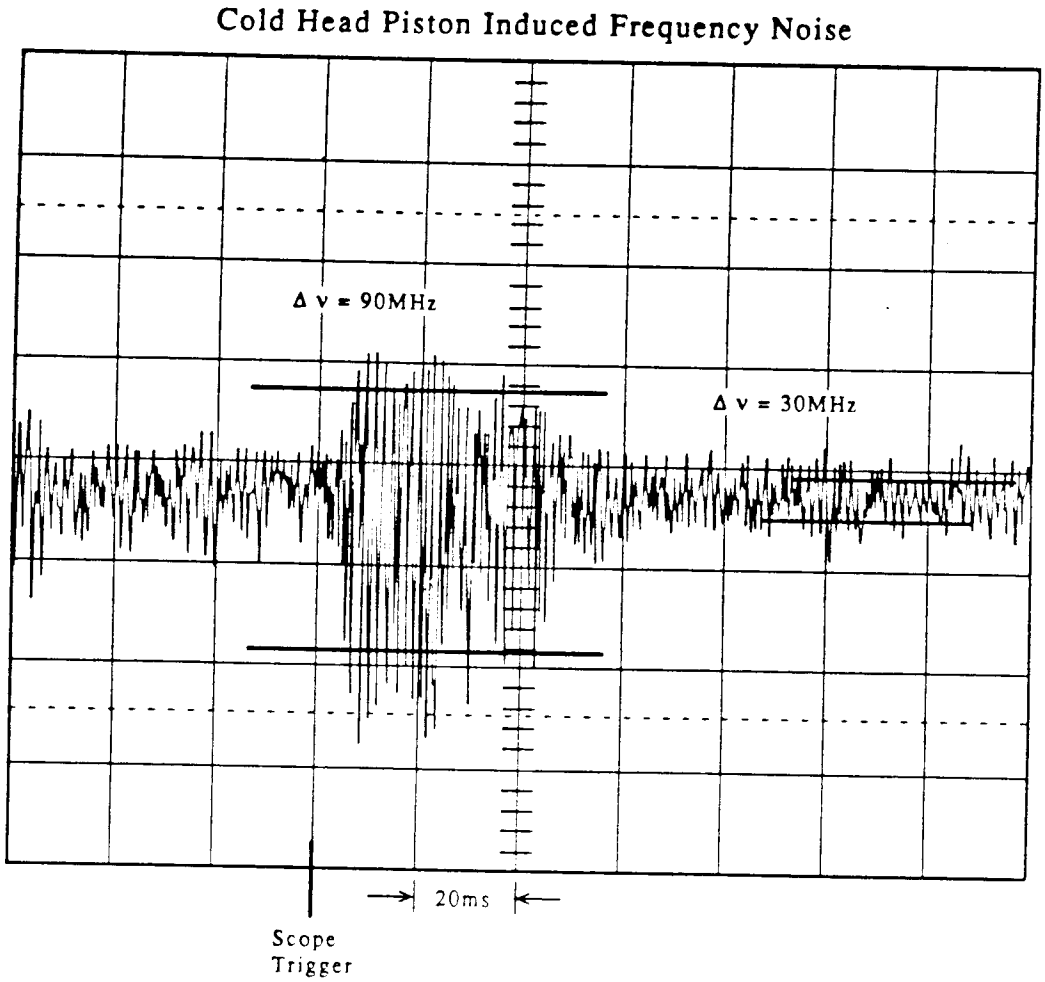

Figure 2.11 Diode laser frequency noise, as determined by selecting a laser frequency which sits on the same of a fringe. The large increase in noise is due to the cold head pistons. A similar burst of noise occurs with each stroke of the pistons in the cold head. In fact, the trace was obtained by triggering the oscilloscope with a microphone placed near the cold head.

diode laser on the side of an etalon transmission fringe and monitoring the amplitude of the transmission signal. The burst of noise in Figure 2.11 is associated with a cycle of the cold head piston. By knowing the slope of the etalon fringe one can obtain a rough measure of this frequency noise. However, a better method to quantify the frequency noise involves measuring accurately the line width of a stable molecule (OCS) in the slit jet. The procedure by which the line widths are measured will be discussed later in this chapter and only the results will be presented here. Since the major sources of line width broadening of stable molecules (eg. OCS) in the slit jet are residual Doppler broadening and frequency noise, by determining the Doppler width and the absorption line width, the frequency noise is measurable. The average FWHM Gaussian absorption line width for OCS transitions is 52(4) MHz. This is substantially larger than the 16 MHz predicted for Doppler width at 8 K. Thus, essentially the entire line width can be attributed to frequency noise. However, it should be stressed here that this measurement is representative of only a small region of possible lasing frequencies, and that the frequency noise varies across this region. The magnitude of this effect is approximated to be about ±10 MHz. Thus, the frequency noise on the diode laser is best represented as 49(10) MHz.

Since the inherent spectral width of species in the jet is less than the observed frequency noise, the absorption sensitivity will be increased if the frequency noise is reduced (due to larger peak absorption strengths). A reduction in the frequency noise has the additional benefit of improving the detection sensitivity to lifetime broadening in spectral transitions. One way to reduce the frequency noise sampled by the experiment is to simply shut off the data acquisition during the periods of excess frequency noise. The disadvantage of such a modification is a loss of about 1/3 of possible data taking time.

An alternate method, which does not suffer from this problem, is to stabilize actively the laser output by feeding a frequency dependent correction back onto the laser through an external current input. The error signal is obtained by selecting the frequency of the diode laser such that it is on the side of a transmission fringe. This signal is passed to a home built servo circuit composed of proportional and integral gain amplifiers (shown in Figure 2.12). Briefly, the circuit is composed of a pure integrator, which rolls off at about 15 kHz. The first element is an integrator at low frequency, providing extra gain, and at about a frequency dictated by R(20kΩ)*C(33nf) it acts as proportional gain. The last two elements are responsible for setting a

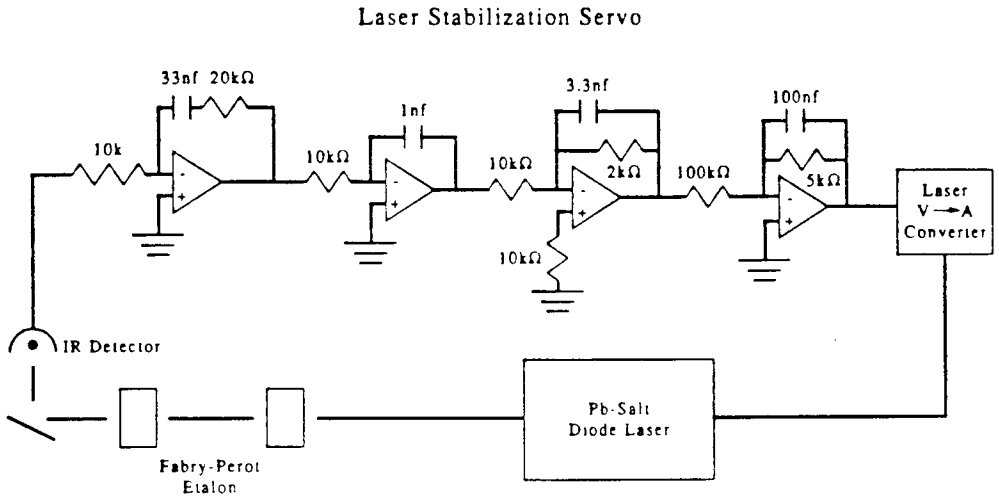

Figure 2.12 The laser stabilization servo. The circuit is composed of one stage of pure integration is included (the second operational amplifier (op. amp.). One stage with a knee (the first op. amp.) for additional gain at low frequency but the gain rolls off and becomes simply proportional gain of 2 at about 240 Hz. The last two op. amps. roll off the gain near DCl which would otherwise be infinite. Also included but not shown is an adjustable gain proportional amplifier.

finite gain at very low frequencies. Additionally, one stage of adjustable proportional gain is included (not shown). The error signal from this circuit is fed back on the laser via an external voltage to current input. This input has a flat response to about 20 kHz. A pure integrator has a phase shift of -90° and a frequency roll-off of -6 dB/octave. Potential problems arise if another source of phase shift is present at frequencies where the gain goes through unity. If this is the case, the circuit will be unstable due to positive feedback.

This technique has been demonstrated to reduce the free running frequency noise of 50 MHz to about 10 MHz. This represents a substantial reduction in the frequency noise which is sufficient to place the frequency noise lower than the residual Doppler width. However, it is not used in everyday data acquisition due to difficulty in frequency scanning. While a piezoelectric crystal is the element of choice to scan the external cavity (and thus the diode laser), one needs to change the cavity length by 1-2 times the wavelength of light. This is difficult to do rapidly (~1 kHz) for 5 μm radiation. Alternatively, a small frequency dither can be applied to the diode laser, which is an often used technique. Intracavity CaF_2 galvo plates are capable of changing the cavity length by the requisite amount, but initial attempts to incorporate them failed since the resultant

etalon fringe height was reduced to an unusable level. Further work is required to make this scheme practical for daily use, but it has been shown to be feasible and represents substantial benefits for future data acquisition.

Optical Layout

The optical layout for the Pb-salt diode laser spectrometer is shown in Figure 2.1. The infrared radiation emitted from the diode laser is collected with an off-axis parabolic mirror with a focal length of 1.5". The advantages of this mirror over a large diameter lens are near unity reflection over most of the infrared and no dispersion, as well as being a parabolic element which will focus off axis with no stigmatism. It is positioned to collimate the highly divergent (≈f/1) diode beam. A number of flat gold turning mirrors are used to redirect the beam (see Figure 2.1). Adjustable irises are used to localize the infrared beam and to facilitate overlap with a visible HeNe tracer beam. The only transmission optics along the beam path are CaF_2 lenses used to 1) focus the beam through a spatial filter (discussed earlier), 2) collimate the beam following the spatial filter, and 3) focus the beam (f/2, 1") onto the infrared detector.

Following the spatial filter, the beam is divided via a pellicle beam splitter. Approximately 10% is

sampled for diagnostics, as discussed below, with the remainder passing through to the molecular expansion. A schematic of the pulsed valve (discussed in more detail later in this chapter), vacuum chamber, and multipass mirrors is shown in Figure 2.13. A small vacuum chamber (6" diameter X 5" tall) is used to simplify laser alignment along the slit axis and to maximize pumping speed. The disadvantage of such a small chamber is that the multipass mirrors can not be placed inside the chamber. Thus, each pass requires transmission through two CaF_2 windows. The optimum number of passes used therefore represents a balance between longer pathlength and the reduction in laser power due to additional losses for each pass.

One can calculate the number of passes which provides the optimal signals given the transmission of the window as follows. First, the observed signal amplitude is expressed in terms of the IR power and number of passes.

$$S \propto P * n \qquad (2.5)$$

where, the signal amplitude is labeled as S, the power as P, and the number of passes as n. If we assume that the only power loss due to multipass is reflection losses at each window surface, the power following any particular

Slit Pulsed Valve and Vacuum Chamber

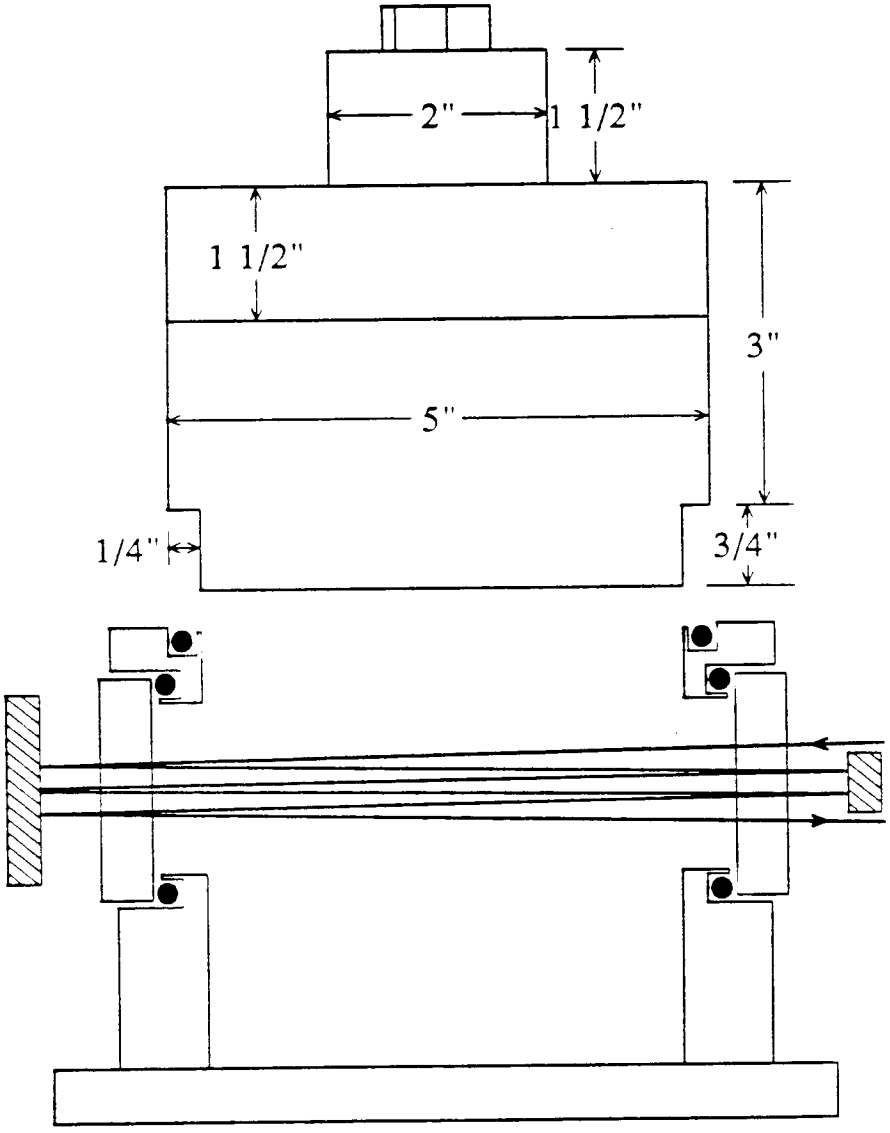

Figure 2.13 Schematic diagram of the pulsed valve and vacuum chamber. As is apparent in this figure the vacuum chamber is quite small, and in fact is only slightly larger than the slit pulsed valve. The slit valve rests on the vacuum chamber and points downwards into a 6" diffusion pump. The six passes typically utilized for these studies are shown. The vacuum chamber windows are either CaF_2 or sapphire, both of which provide essentially identical behavior, except sapphire windows (1 mm) are thinner than CaF_2 (8 mm).

number of passes (n) is expressed as

$$P_n = P_0 \ (T)^{2n} \tag{2.6}$$

This loss is due to both absorption of the infrared light by the optical material and scattering off each of the interfaces. The exponent is 2n rather than n since each pass requires transmission through 2 windows (4 surfaces). The signal, as a function of T and n, is given by Eq. 2.7.

$$S \ \alpha \ n \ T^{2n} \tag{2.7}$$

Eq. 2.7 is maximized with respect to n by taking its derivative and setting it equal to 0.

$$\frac{\partial}{\partial n} \left[n T^{2n} \right] = 2n \ \ell n(T) \ T^{2n} + T^{2n} = 0 \tag{2.8}$$

Solving for n yields,

$$n = -\frac{1}{2 \ \ell n(T)} \tag{2.9}$$

Using a typical transmission through a CaF_2 window of

about 94% (T=0.94) leads to a prediction of 8 passes for the optimum signal. However, the windows on the vacuum chamber are coated with a thin diffusion pump oil film while running which can further reduce the transmission. A liquid N_2 trap is not used since it reduces the effective pumping speed below an acceptable level. A slight reduction to T=0.9 lowers the optimum conditions to 4-5 passes. Thus, six passes were used for all experiments reported herein. Following the multipass, which is formed by two flat mirrors as shown in Figure 2.13, the infrared beam is focussed onto HgCdTe detectors, discussed below. Reference beam subtraction (as is utilized with the difference frequency spectrometer) is not used in this experimental arrangement. While fixed frequency advantages of about a factor of up to 20 in absorption sensitivity are obtained with dual beam subtraction of the diode laser source, this advantage is lost very quickly when the frequency is changed. We believe this is due to difficulties with slight beam steering concurrent with frequency scans, and amplitude noise written on the signal beam due to the multipass which is not coherent with respect to any reference beam noise.

The two types of infrared detectors used with this apparatus are indium antimonide (InSb) and mercury cadmium telluride (HgCdTe). A 1.0 mm^2 HgCdTe detector is

used for signal observation. This is a photoconductive detector, purchased from Infrared Associates, model number HCT-90, which is inherently AC coupled and is used with an amplifier also from Infrared Associates (model PPA-15-10). The amplifier is powered by 15 volt rechargeable gel cell batteries. The detector and amplifier pair has a total responsivity of 3 X 10^5 V/W in a band width of 10 Hz to 10 MHz. The detector has a peak detectivity at about 10 μm of 3.4 x 10^{10} cm $Hz^{1/2}/W$ in a 1 kHz bandwidth. At about 5 μm where these studies are carried out, the sensitivity per Watt is down by about a factor of two.

The other detectors used are photovoltaic InSb. These were assembled in-house from InSb elements. The wafers are fixed to copper base plates (see Figure 2.14) with a thin film of indium. These Cu plates also serve as the ground plane for the detectors. The output is amplified by home built transimpedence amplifiers (see Figure 2.15) with a switchable total gain of either 10 kΩ or 1 MΩ. While the output of these detectors is capable of DC operation, the high gain setting requires AC coupling (at about 5 Hz) due to residual DC offsets in the amplifiers. These are large area detectors (about 4 mm^2) which saturate with black body radiation from the laboratory. Therefore, an AR coated Ge window, cooled to liquid N_2 temperature, is placed in front of the detector

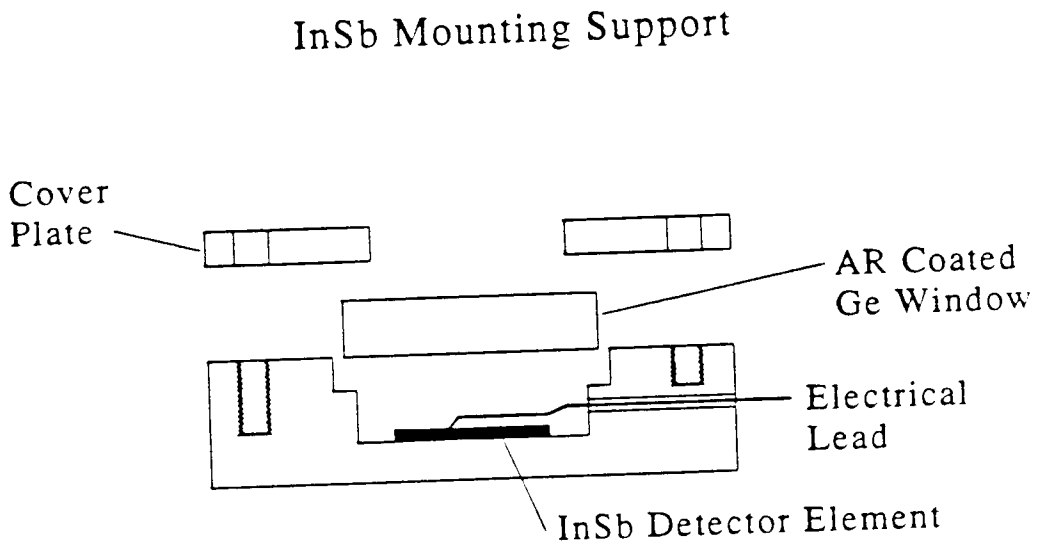

Figure 2.14 The home-built mounting support for InSb detector chips. The whole assembly is construct of Cu to maximize both thermal and electrical conduction. A small wire is attached to the center of the detector element. The back surface of the element serves as ground and is attached to the Cu mount via a thin layer of In. A Ge window is placed in front of the detector and cooled to 77 K to reduce black body radiation impinging on the detector.

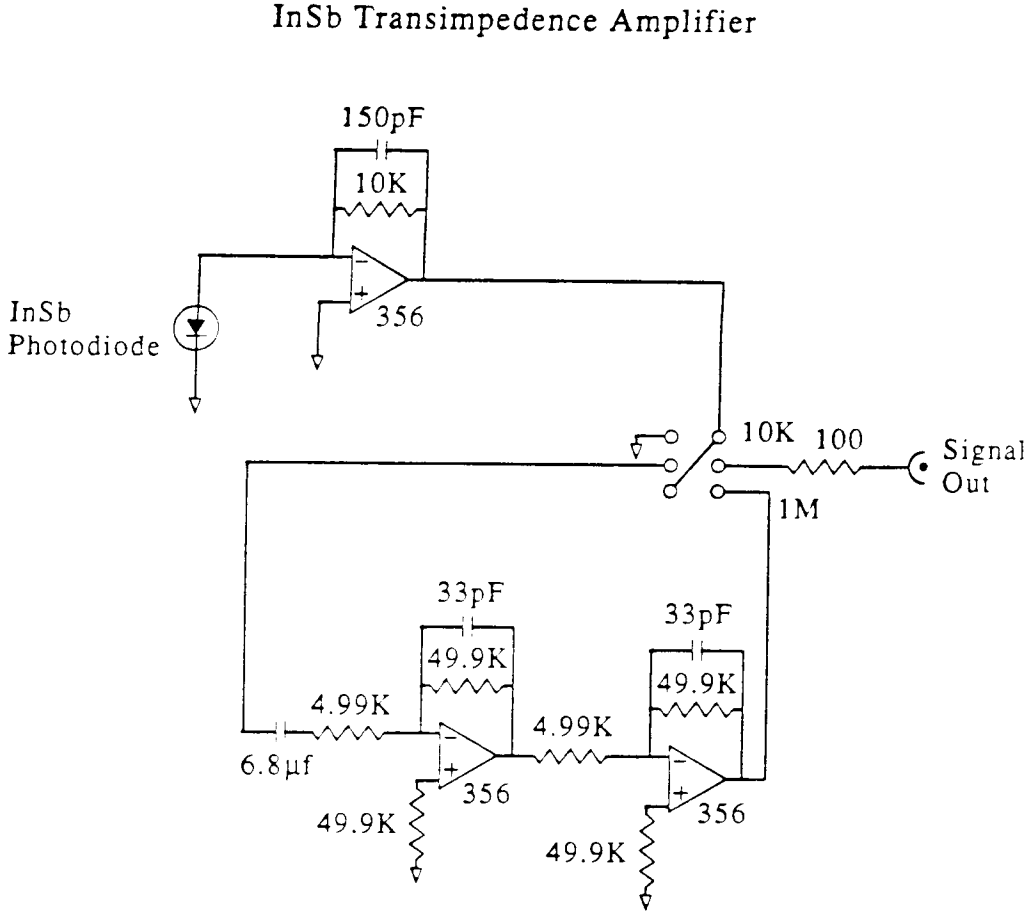

Figure 2.15 The transimpedance amplifier used for the InSb infrared detectors. The op. amp. shown at top is the actual transimpedance amplifier with a gain of 10 kΩ. The other two amplifiers provide additional gain if so desired. The output can be selected to come either directly from the transimpedance amplifier or after the two additional stages of gain. Since each of these amplifiers provides a factor of 10 gain, the final output has a gain of either 10 KΩ or 1 MΩ. Due to offset drifts in the two extra amplifiers, this signal is AC coupled with the 6.8 μf capacitor.

element to reduce the effects of black body radiation. Since this radiation depends on T^4, a reduction from room temperature to 77 K is a significant improvement, also the Ge filter is quite small (5 mm) and placed about a cm away from the detector element thus reducing the clear aperture.

Signal Detection and Analysis

The data acquisition is controlled by a basic program called SCANBELL.BAS (see Appendix I for a listing). This program calls a number of in-house written assembly language subroutines which are listed in Appendix II. Briefly, transient signals are averaged on a digital oscilloscope and then sent to the computer for integration.

The basic program initializes a Scientific Solutions (#800022), D/A board to start a train of pulses. Once initiated, those pulses run unimpeded. A voltage ramp, supplied by the D/A board, is passed to the voltage to current converter to scan the laser frequency. An assembly language subroutine VOUT.ASM (see Appendix II) drives the voltage ramp. The train of pulses from the D/A board triggers both the pulsed valve and the digital oscilloscope. The AC coupled output of the HgCdTe detector (discussed above) is band pass filtered with 6 dB points at 100 Hz and 3.5 kHz and recorded on a

digital storage oscilloscope (Tektronix model 2430A). The scope is operated in a data averaging mode, i.e. the oscilloscope runs independently until it has averaged a specified number of slit valve pulses. Upon completion of this average, the scope signals the computer to acquire the waveform, which is sent to the computer over a GPIB bus in the "fast transmit mode" option of the Tektronix scope.

Active baseline subtraction is used as follows: Two baseline gates are positioned on either side of the centrally located signal gate (see Figure 2.16). These baseline gates are each 256 channels long and separated from the signal gate by 100 channels. A straight line is least squares fit to each baseline gate (see subroutine SUM.ASM in Appendix II). The baseline for integration is determined by the line connecting the point where the baseline extrapolated straight lines intersect the signal gate, labelled a-b in Figure 2.16. The actual integration is also carried out within the subroutine SUM.ASM, and involves simply adding the value of each data point in the signal gate minus the value of the baseline at that point. This active baseline subtraction yields an output which is insensitive to amplitude noise on the ~1 msec time constant or longer. The spectrometer absorption sensitivity of 6×10^{-4} is routinely obtained and results in a detection limit of 2.0×10^{10} DCl

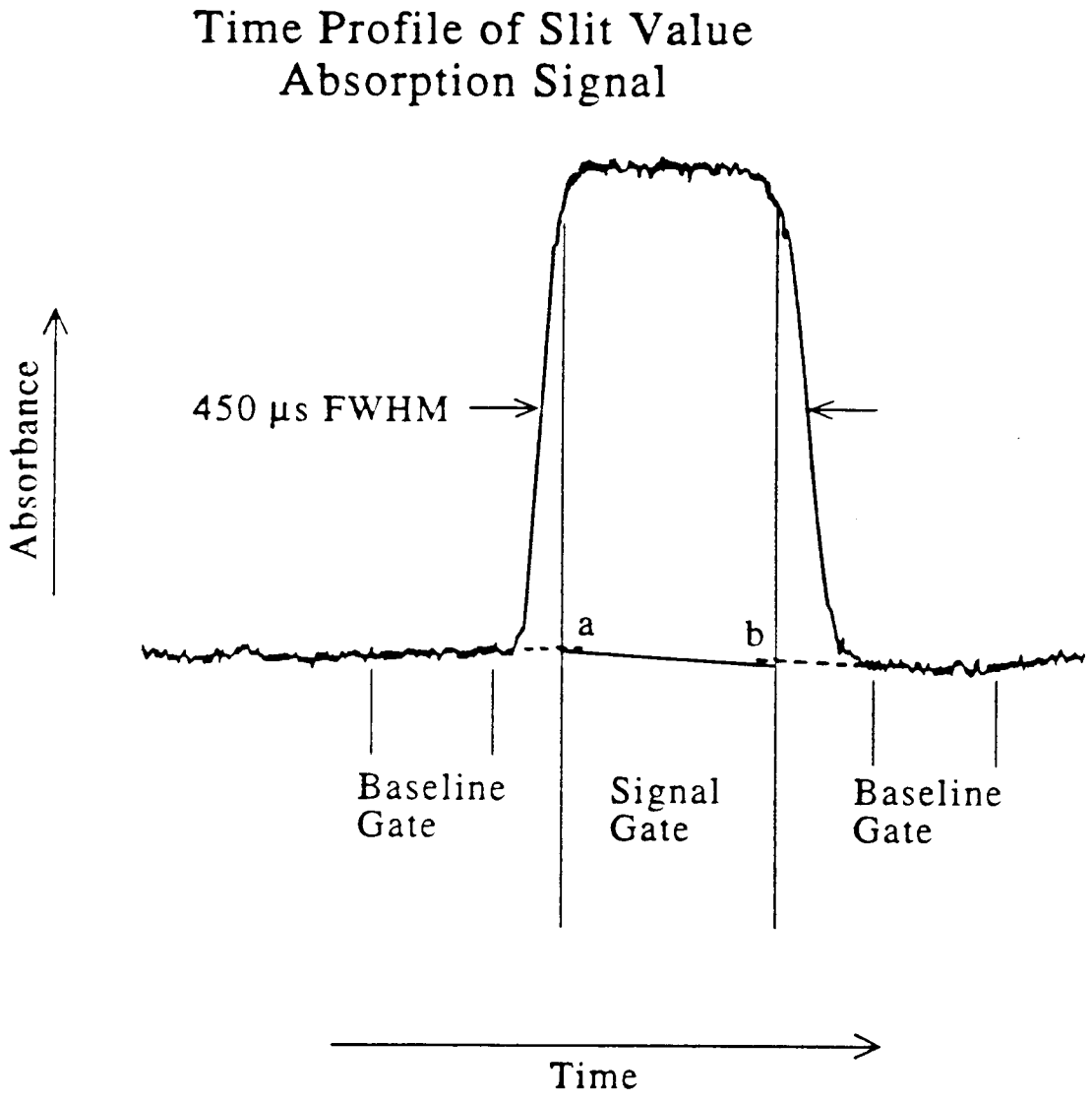

Figure 2.16 A time trace of a typical absorption signal obtained on the difference frequency spectrometer. The signal is flat across the top and exhibits a turn-on and turn-off time of 50-75 μs. Baseline gates are determined by fitting straight lines to regions of data outside the absorption range. The points at which these straight lines intersect the edges of the signal gate determine the baseline for integration (the line a-b).

containing complexes/cm^3/quantum state based on a transition moment of the complex equal to that of free DCl.

The absolute frequencies for the observed absorption signals are determined with a combination of a reference gas absorption cell and a fixed length Fabry-Perot cavity. About 10% of the total power is used for the gas cell and etalon. This fraction is further split with about 9% of the total power going to the reference cell and 1% to etalon, which represents sufficient power to provide S/N of >100 for both reference and etalon signals. Both are obtained by chopping the IR beam at about 300 Hz with a mechanical chopper and collecting the signals with lock-in detectors (Stanford Research Systems Model 510). The lock-in reference signal is supplied by a HeNe laser which is chopped simultaneously with the diagnostic beams and focused on an FND-100 Si photodiode.

The etalon is formed from 95% reflective flat mirrors spaced (ZnSe substrate) by about 25 cm, providing a free spectral range (FSR) of about 635 MHz and a finesse of 10-15. Since the back surfaces of the etalon optics are uncoated, about 3% is reflected back toward the laser. If more than about 5% of the total power is put on the etalon, enough of this reflected light gets back to the laser source to cause an observable increase in frequency noise.

The etalon fringes serve two purposes in this experiment. First, the fringes are used to indicate the presence of multiple longitudinal modes when searching for optimal temperature/current conditions for a particular frequency region. This search is carried out by scanning the laser current about 0.1 - 0.5 cm^{-1} in a rapid scan utilizing the internal sawtooth mode of the current supply. Secondary mode fringes are well separated from those of the primary mode and are readily observable if the secondary mode power is greater than about 10% of the total power.

Secondly, and more importantly, the transmission fringes are used to interpolate the unknown absorption peak frequencies from those of a reference gas. Carbonyl Sulfide (OCS) absorption frequencies are used for the absolute frequency standard for all studies reported herein. The OCS gas is contained in a static cell, and the attenuation of the laser beam is monitored with a lock-in detector as discussed above. The transition frequencies are reported by Hunt et al.[11] to an accuracy of 0.0003 cm^{-1}. Two such OCS peaks are used to calibrate the etalon FSR for each spectral scan. The unknown frequency positions are then interpolated from two or more nearby OCS positions. Multiple scans over the same frequency regions are recorded and the results averaged to reduce the effects of random errors. This procedure

provides a reproducibility of ±0.0005 cm^{-1}, as determined by comparisons with multiple OCS reference gas transitions. The convolution of our precision with the quote accuracy of the OCS measurements yield an absolute accuracy of ±0.0006 cm^{-1}.

Difference Frequency Laser Spectrometer

The fundamental principle behind the difference frequency laser spectrometer (shown in Figure 2.17) is the nonlinear mixing of two visible lasers[11].

$$\omega_1 = \omega_3 - \omega_2 \qquad (2.10)$$

The highest frequency (ω_3) laser is a Spectra Physics 2020 Ar^+ laser with an internal temperature stabilized etalon. While this laser will lase on either blue (488.0 nm or 20486.8 cm^{-1}) or green (514.5 mn or 19429.2 cm^{-1}) transitions, all spectra herein were taken with the green line. Single frequency outputs of 0.8 W with a frequency stability of 1 MHz are routinely available with this laser.

The output of the Ar^+ laser is mixed with the single frequency output of a Spectra Physics 380A dye laser, pumped by a 4 W Spectra Physics 2020-05 Ar^+ laser. Dye laser output powers of 0.2 - 0.5 W are achieved with Rhodamine 6G dye. The dye laser has been modified slightly to provide active frequency stabilization, via

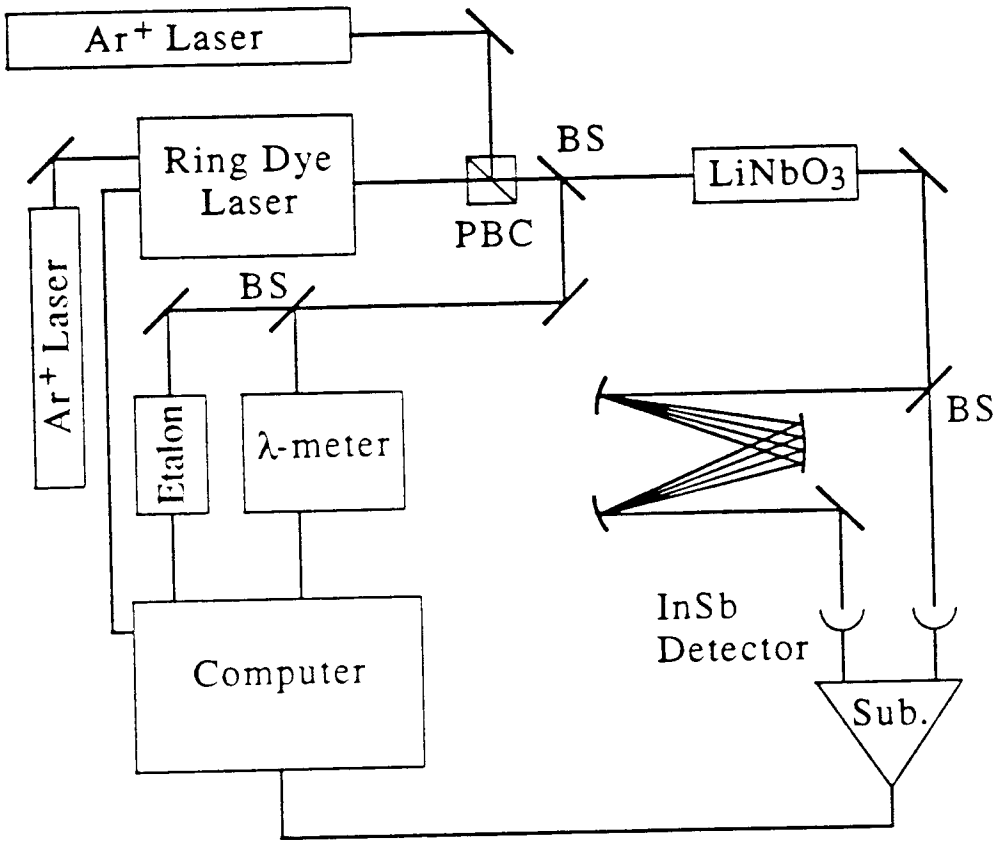

Figure 2.17 A schematic layout of the difference frequency laser spectrometer. The outputs of a single frequency Ar^+ and ring dye lasers are overlapped and passed into a $LiNbO_3$ crystal. A small amount of infrared light at the difference frequency is produced. This beam is split with 50% going to a White cell multipass through the slit jet expansion and the remainder serving as the reference beam. The outputs of the signal detector is subtracted from that of the reference detector, the result being sent to a transient digitizer.

insertion of a piezoelectric crystal (PZT) behind one of the cavity mirrors[8]. A fraction of the output power is passed into an external Fabry-Perot etalon which is equipped with a piezo driven end mirror. The dye laser is forced to lock to one side of a cavity etalon fringe. Scanning is accomplished by slowly changing the external cavity length via a voltage ramp to the PZT. Since the PZT scan is slightly nonlinear, the resulting spectral scan is nonlinear, as evidenced by about a 10% difference in channel numbers between dye laser etalon fringes near the beginning of a scan and near the end. The frequency of the dye laser is then pulled along with the external cavity producing scans of up to about 2.5 cm^{-1} in length. This technique reduces the frequency noise on the dye laser from the free running value of about 50 MHz to about 3 MHz in a 2 kHz bandwidth.

The horizontally polarized dye laser and vertically polarized Ar^{+} laser are combined with a polarization beam splitter and rendered collinear via alignment through variable diameter irises. The visible lasers are focused into a $LiNbO_3$ crystal via a 20 cm focal length achromatic lens. The crystal is cut and positioned for 90° phase matching of the visible lasers. The correct phase matching conditions are maintained throughout a spectral scan by adjusting the crystal temperature which is controlled to ±0.05° via active stabilization by

comparison with a reference thermocouple junction. Because $LiNbO_3$ will transmit from visible to only 4.2 μm, the crystal itself is responsible for the long wavelength limit of the difference frequency spectrometer. Conversely, the short wavelength extreme (2.2 μm) is determined by the lowest temperature at which the $LiNbO_3$ crystal can operate and not suffer index damage due to absorption of the Ar^+ laser. This damage is prevented at higher temperatures as a result of self annealing in the crystal.

The resulting IR beam (power $\leq 10^{-5}$ W) is focused with a 10 cm focal length CaF_2 lens and then split; approximately 50% is used for a reference beam and 50% for signal detection. The signal beam is passed into a White cell[12] multipass arrangement. In this optical layout, end mirrors (gold coated pyrex substrates) are separated by their radius of curvature (30 cm). The beam is focussed at the input mirror (M1) and refocussed on this mirror with each pass. The infrared beam is typically multipassed through the White cell either 12 or 16 times and then focussed on the signal detector.

Both the signal and reference detectors are photovoltaic InSb with an active area of 0.049 mm^2. The current signals produced by the detectors are converted to voltages via transimpedence amplifiers (identical in principal to that shown in Fig 2.15 with a total gain of

10^5 Ω. These amplifiers are assembled in-house using components carefully chosen to match the frequency responses as closely as possible. The outputs of the signal and reference detectors are subtracted, thus reducing the IR amplitude noise to about 1-2 x 10^{-4} of the incident light level, within a factor of 2-3 of the shot noise limit in a 5 kHz band width for about 5 μW of IR power.

Absorption signals are concurrent with the pulsed valve and are monitored via attenuation of light reaching the signal detector . The infrared signal recorded during each valve pulse is displayed on an oscilloscope and averaged with a transient digitizer (DSP Technology Model 2001S). Typically, four pulses are summed together to increase the S/N. This sum is then passed to a personal computer for integration with baseline subtraction providing a detection sensitivity of 10^{-6} absorption/ $Hz^{1/2}$ per single gas pulse in a 5 kHz band width. This corresponds to a detection limit of 1 x 10^8 HCl containing complexes/cm^3/quantum state. This detection limit is 200-fold smaller than that for the diode laser. This is due to 1) 6-fold higher sensitivity, 2) the 2.5-fold larger HCl absorption strength, 3) the 2-fold narrower line width, 4) the 2-fold longer pathlength, and 5) the ability to cool all HCl molecules into J=0, but not DCl. Simultaneously, the

computer records both dye laser transmission etalon fringes from a fixed length external cavity and the infrared power measured on the signal detector. These data are collected through A-D ports read directly by the computer.

Once signals are observed, the absolute frequencies must be determined for each transition. A home built traveling Michelson interferometer, referred to as a "lambda meter", is used for this task. The apparatus is shown in Figure 2.18 and is based on the original design of Lee and Hall[13]. The scheme involves separating the laser beam of interest with a 50% beam splitter, and passing each fraction through a different arm of the interferometer. Interference fringes are collected (see Figure 2.19) as the cart travels from one extreme to the other (40 cm in our apparatus). The ratio of interference fringes counted in a certain time interval from the light of interest to those of a reference polarization stabilized HeNe laser is equal to the ratio of wavelengths for the two lasers. Since only an integral number of wavelengths can be measured, the error associated with this measurement is as large as 1 count out of about 1 X 10^6 total counts, or an error of 1 part in 10^6. This error is reduced by increasing the number of counts via a phase lock loop which multiplies the count rate by as much as 16, thus reducing this error to

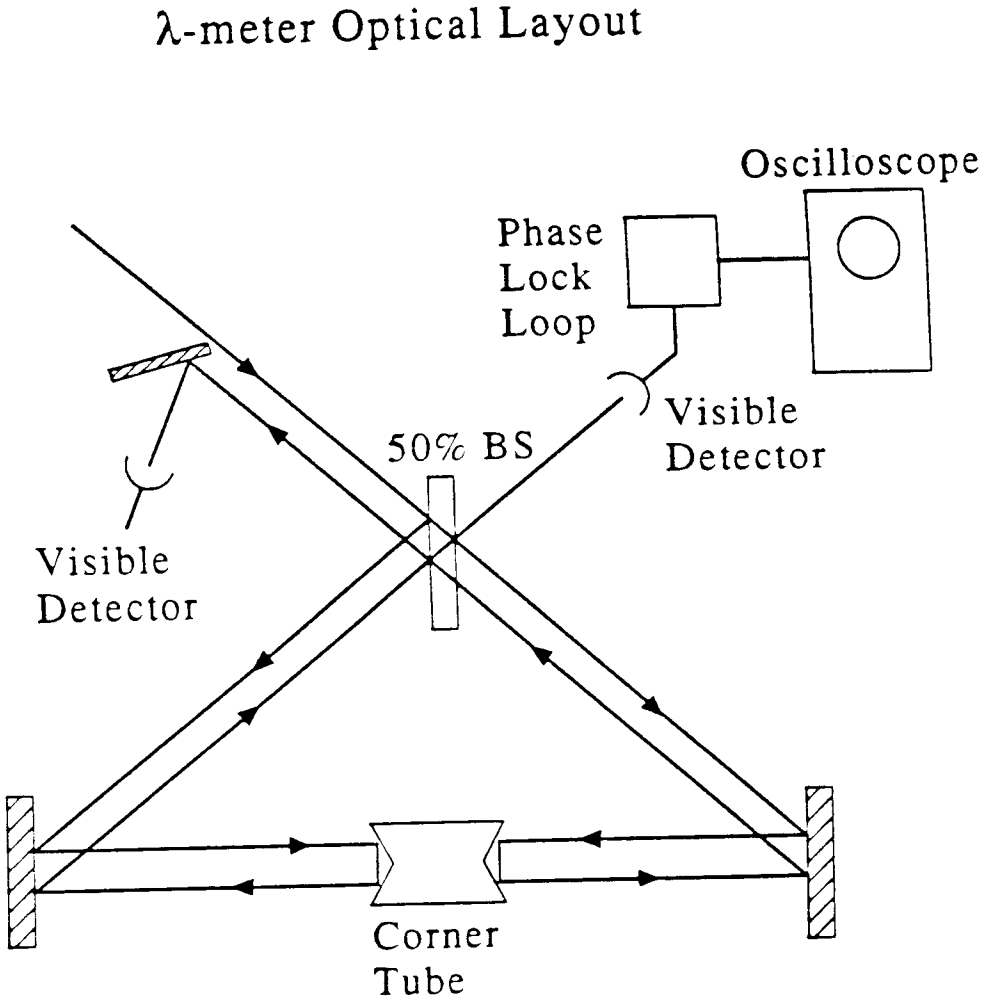

Figure 2.18 The optical layout for the λ-meter, which is used for frequency measurement. A 50% beam splitter divides the beam into equal parts, which ravel the separate arms of the interferometer. When the beams are recombined, they interfere and produce fringes at a frequency determined by the wavelength of light and the cart speed. The optical paths are folded with a corner cube, which is shown near the bottom of the figure. This corner cube rides on an air bearing to provide a near constant cart speed.

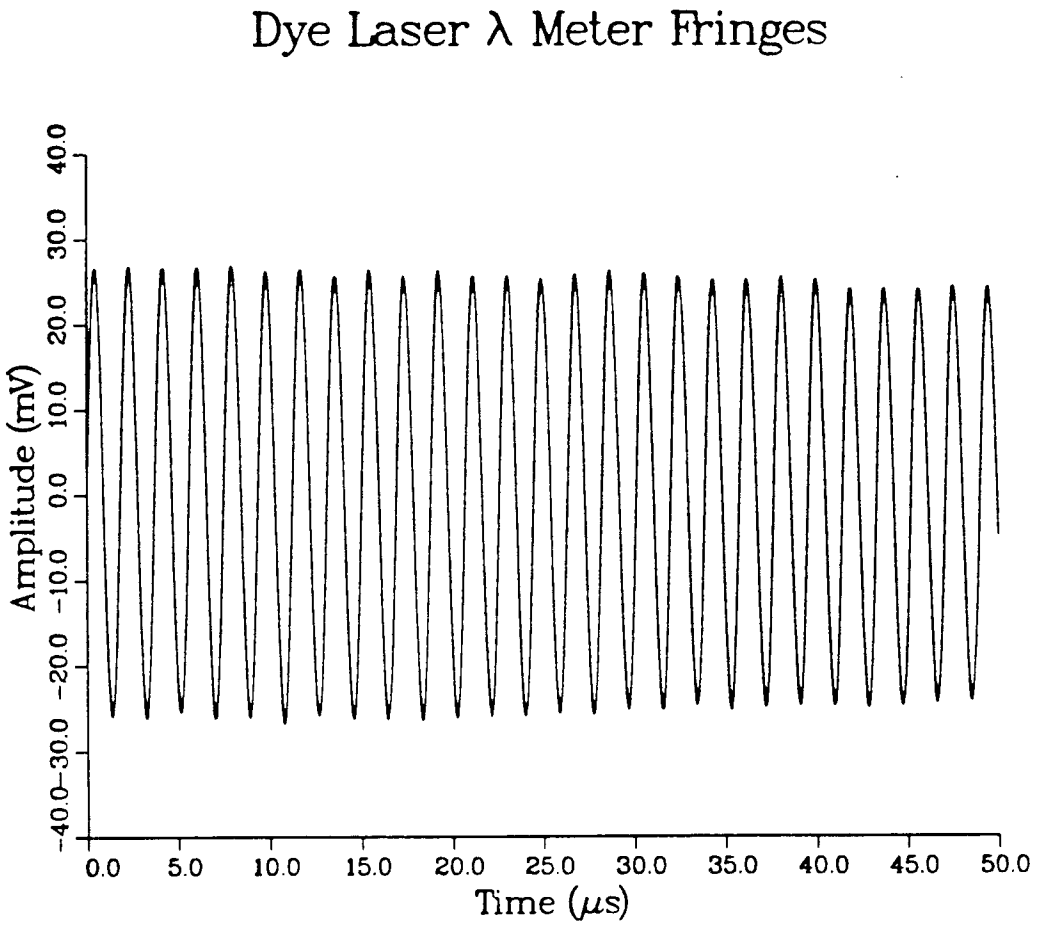

Figure 2.19 An example of the λ-meter fringes obtained for the dye laser, with similar fringes observed for both the Ar^+ and HeNe light. The frequencies of both the Ar^+ and dye lasers is determined from the ratio of zero counts for these lasers to that of a reference frequency stabilized HeNe laser.

less than 1 part in 10^7, or about 0.001 cm^{-1}, for each reading of the lambda meter for the visible lasers. As discussed below, several repetitive readings are made to reduce this uncertainty even further.

To convert this wavelength to frequency requires an accurate knowledge of the index of refraction of air, which is far too sensitive a function of temperature and color for our purposes. Instead, the absolute infrared frequency is determined via observation of reference gas transitions (eg. HCl^7 or HF^{14}) for molecules seeded into the supersonic expansion. This provides an infrared frequency correction due to the small uncertainties in the HeNe frequency and index of refraction. Since the HeNe frequency is stable to ±2 MHz over several hours, and the room temperature varies only slightly over a day (<5 °C), this frequency correction is useful for an extended period of time. One could use a reference gas cell similar to that used with the diode laser spectrometer, but there are not as many likely candidates for reference gases in this region of the spectrum (2 - 4 μm). Additionally, most of the molecules (eg. CH_4, HF, H_2O) which could serve as reference gases have large rotational constants, and thus rotational spacings ≥1 cm^{-1}. One is then forced to interpolate a significant distance to cover all of the spectral scan.

Since lambda meter conditions (eg. alignment and

room temperature) change from day to day, the lambda meter must be calibrated daily. This involves repeatedly measuring the apparent transition frequency in the slit jet to determine the correction factor, i.e. measured transition frequency minus the true frequency[7,14]. By averaging about 40 measurements, a residual standard deviation of the mean of about 0.0002 cm^{-1} is obtained for determination of the correction factor (0.0416 cm^{-1}). This correction factor changes slightly from day to day, but is never more than about 1% unless the lambda meter is realigned in which case it may vary by up to 1-3%.

The van der Waals transition frequencies can be determined using the same procedure as for the reference gas transitions. However, due to the significant number of van der Waals transitions observed (eg. over 1200 for HCl dimer alone), not all van der Waals transition frequencies are measured directly in this manner. The frequencies of these absorption peaks are determined by interpolation from lambda meter determined frequencies utilizing the dye laser transmission fringes. The free spectral range of this cavity (ca. 322.3 MHz) is determined by calibration with two peaks on a particular scan which have been measured interferometrically. The absolute frequency accuracy for peak position determined in this manner is ±0.0005 cm^{-1}, or ±15 MHz, as determined by comparing interpolated reference gas positions with

the published values[7,14].

Slit Pulsed Valve and Gas Handling

The study of van der Waals complexes requires an efficient means to synthesize these weakly bound species. A supersonic expansion, with its high number density and low rotational and vibrational temperatures, has proven to be one of the most useful means of synthesizing these complexes. Additionally, the slit jet geometry provides a long absorption pathlength as compared with a pinhole expansion. The single pass absorption pathlength in the slit used for these experiments (4 cm) provides about a 400-fold increase in path length over that of a 100 μm diameter pinhole. A multipass, of course, can further increase the path length; 12 passes for a total path length of 48 cm are used for these studies. Additionally, since a slit jet only expands perpendicular to the slit axis, the density of gas falls off as $1/r$, rather than the $1/r^2$ drop off in density for a pinhole which expands in two directions. This provides a higher number density and more collisions than for the pinhole expansion with the same backing pressure. The slit has an additional advantage that the molecules do not expand along the long axis, thus the Doppler frequency shifts are quite small for the slit expansion (eg. 25 MHz FWHM

measured for ArHCl transitions with 400 torr backing pressure.

One further benefit of the slit jets, discovered only after having studied a number of systems, is that the vibrational, rotational, and translational modes tend to be in equilibrium at a common temperature. This presumably results from the large number of collisions in the slit expansion. This equilibrium property of slit expansions has been exploited in the HCl-DCl / DCl-HCl systems to obtain a measure of the energy difference between the two conformers, as will be discussed in Chapter VI.

One disadvantage of a slit expansion is that for the same backing pressure behind the expansion, the pumping requirements for a slit expansion are considerably greater than those for a pinhole. This is a direct result of the 500-fold larger area for a slit, 4.0 cm X 100 μm = 0.04 cm^2, than a 100 μm pinhole with area = 8×10^{-5} cm^2. With the 0.04 cm^2 slit and 500 torr backing pressure (optimal for HCl dimer studies), the gas flow is about 400 torr-liter/sec. The available pumping system for the diode laser spectrometer (6" diffusion pump with mechanical backing pump) has a maximum throughput of only 4 torr-liter/sec. Thus, the valve is pulsed at about 20 Hz with 400 μs long pulses yielding a 1% duty cycle.

The important criteria is whether or not the

pressure in the vacuum chamber is sufficiently low to avoid "shocking" the expansion. This is accompanied by a warming of the species in the expansion to near room temperature, a phenomenon which is not observed with the slit jet under typical expansion conditions.

Operating the valve in a pulsed manner has significant advantages. Primarily, since the valve is only open for a short period of time (typically about Δt=400 μsec), the absorption signal lies at $1/(2*\Delta t)$, or about 1.2 kHz. Moving the signal from near DC to 1 kHz pushes this signal above the main sources of noise on the lasers, such as slow fluctuations in the IR power.

The pulsed slit valve used in these studies was developed in our laboratory and has been discussed in detail in previous publications[15]. A schematic of the valve is shown in Figure 2.20. The seal is made between a viton o-ring stretched into a linear channel, and a knife edge stainless steel base plate. The actual slit is formed by two aluminum half plates bolted to the bottom of the stainless base plate. The valve is opened by momentum transfer from a preaccelerated ferromagnetic plug to a rod on which the viton seal is attached. The viton is then pulled off the knife edge and returned by a compressed spring. A pair of leaf springs attached to the viton holder maintain its orientation relative to the slit. Slit geometries of 75 or 100 μm by 4 cm, and pulse

Pulsed Slit Valve Schematic

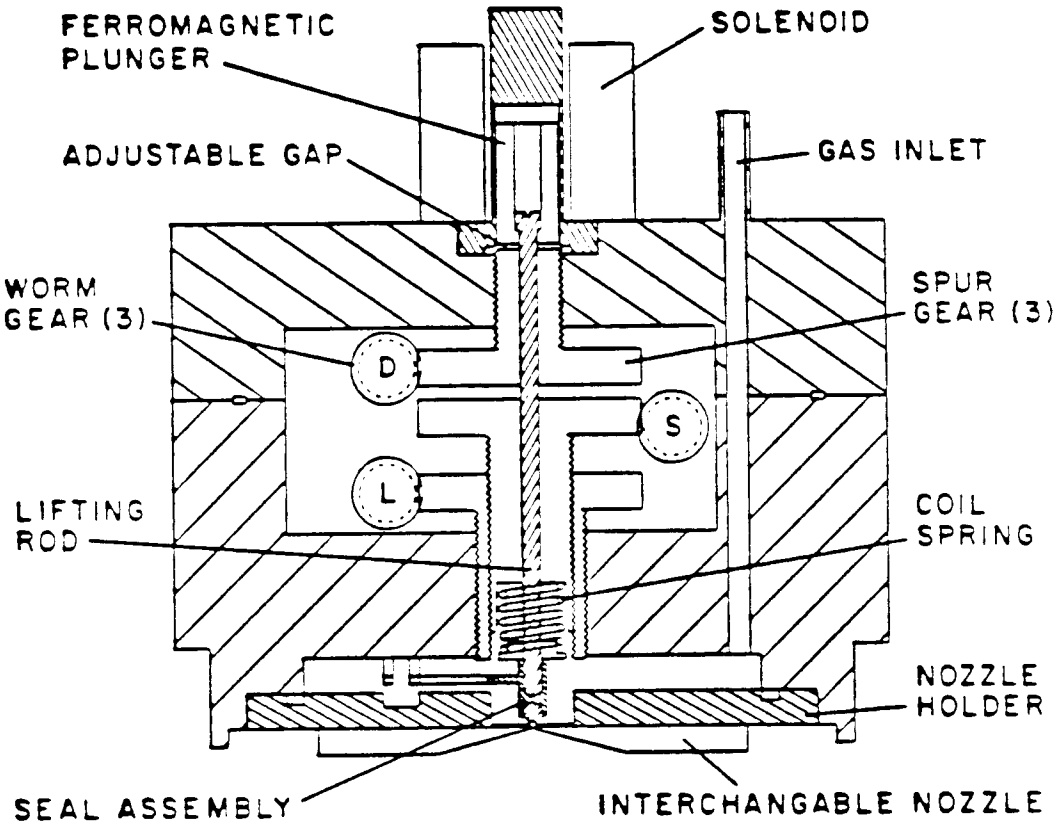

Figure 2.20 A schematic representation of the pulsed value. The actual seal is made between a Viton o-ring and a raised knife edge at the bottom of the valve. Just above this is a compressed spring which is responsible for closing the value. The valve is opened via momentum transfer from a preaccelarated ferromagnetic plug to the rod connected to the o-ring seal. Three worm gears labeled D, L and S for delay, pulse length and spring tension respectively are connected to feedthroughs to allow external adjustment of these parameters. All parts of the valve are constructed of stainless steel except the interchangeable nozzle, shown at the bottom.

lengths of 400-500 μsec are used for all studies expect the NeDCl. Efficient production of this especially weakly bound species requires higher backing pressure and an associated reduction in the pulse length to 300 - 350 μsec in order to minimize the gas load. Feedthroughs, which connect with worm gears inside the valve permit the pulse length, as well as the delay and spring tension, to be adjusted while the valve is operating. The turn-on and turn-off times for the gas pulses are approximately 50 μsec, as can be seen in Figure 2.16.

Two pairs of 1/4" holes drilled through the body of the valve will accept either tube heaters or pipe thread fittings so that a coolant can be circulated through the valve. The production of weakly bound van der Waals complexes such as NeDCl[1] is enhanced greatly by precooling the expanding gas. Either cold water (5°C = 278 K) or cooled ethanol (-60°C = 213 K) is used for this purpose.

The solenoid requires approximately 300 V, 40 Amp electrical pulses to completely open the valve. These are provided by a home built driver circuit based on dumping a large amount of charge stored on an 840 μf capacitor through the pulsed valve solenoid. Silicon controlled rectifiers, triggered by a pulse from the computer, are used to initiate the charge flow. This circuit produces a current pulse of about 200 μsec in

length which can drive the slit valve at a repetition rate as high as 25 Hz.

The partial pressures of the constituents flowing through the valve are varied via flow controllers and are adjusted to maximize the absorptions of van der Waals molecules. Once an optimal mixture is determined, stainless steel or aluminum tanks are used to premix up to 200 standard liters of gas. The gas mixtures found to provide maximum signals for each of the complexes studied are presented in each chapter.

All gas lines are stainless steel and only VCR type fittings are used for connections. Needle valves and a pressure regulator are used to control the stagnation pressure. The exception to this is when studying DCl complexes; the regulator is bypassed and only a needle valve is used to regulate the backing pressure in order to minimize the DCl loss. Additionally, the DCl studies require seasoning of the gas lines with DF to displace any hydrogen containing molecules with those containing deuterium. DF is chosen since we can easily synthesize DF by mixing eximer laser grade F_2 with an excess of D_2 in our mixing tanks. The DF is then separated from the residual D_2 by freezing it out in a liquid N_2 trap. Deuteration of the gas lines and mixing tank is maintained by always keeping them above atmospheric pressure.

All rare gases used in the expansions are used as purchased; i.e. Ar (99.995% purity), Ne (75% Ne, 25% He), and He (99.995% purity). The grade of Ne is referred to as "first run" and is used since it is substantially less expensive than high purity Ne. Both HCl (99.9% pure) and DCl (99% isotopic purity) are freeze-pump-thawed multiple times to remove volatile contaminants.

Line Width Measurements

Infrared excitation of DCl or HCl within a van der Waals complex deposits approximately 2100 or 2900 cm^{-1} of energy into the respective complex. This energy is considerably larger than the binding energy for these complexes of between 100 - 500 cm^{-1}. Of interest is the time scale required to redistribute the H(D)Cl vibrational energy into the van der Waals bond. As the lifetime of a complex is reduced, the corresponding absorption line width will be increased. The ability to accurately measure the increase in line width due to predissociation broadening requires a knowledge of other sources of line width broadening.

The most important source of broadening in the diode spectrometer is frequency noise [49(10) MHz]. The large uncertainty in the frequency noise rivals the expected contribution to line width broadening by predissociation,

and it is therefore very difficult to quantify this source of broadening with the diode laser spectrometer. All line width measurements made on the diode laser are presented as lower limits to the vibrationally excited lifetimes. Active frequency stabilization has been demonstrated to reduce the line width by 3-fold, which should improve these measurements.

Accurate line width measurements are possible on the difference frequency spectrometer. A detailed discussion of the sources of line broadening has been presented by Lovejoy[7] and will only be briefly discussed here. The contributions to the line width due to pressure broadening and transit time broadening are expected to be negligible for all expansion conditions with <1000 torr backing pressures. However, Doppler broadening is observed in the slit jet, as evidenced by 29 MHz line widths for ArHCl at 10 K. Doppler broadening increases the heterogeneous line width, thus, the effects of Doppler broadening are manifested in an increased Gaussian component to the line shape. This contribution is quantified by scanning over absorptions due to either stable molecules (eg. CH_4 or HCl) or long lived van der Waals molecules (eg. ArHCl) in the slit jet. Figure 2.21 shows a line shape fit to a methane Q branch transition. The fitted line shape is Gaussian with a FWHM of 63.8(14) MHz. The line shapes of these stable species in the jet

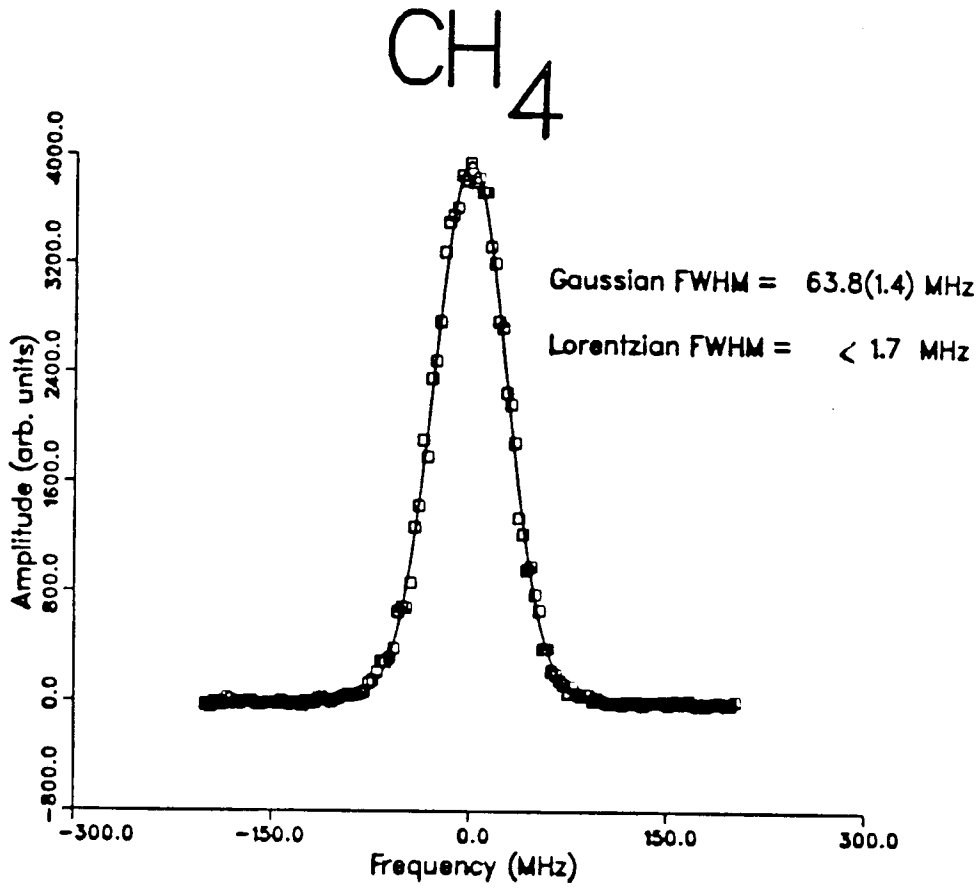

Figure 2.21 Line shape fit to a methane transition in the slit jet. This transition is fit quantitatively to a Gaussian line shape with < 1.7 MHz Lorentzian component. The line width of this CH_4 transition is 2-fold larger than that of $(HCl)_2$ transitions due to the light mass of the CH_4 molecule.

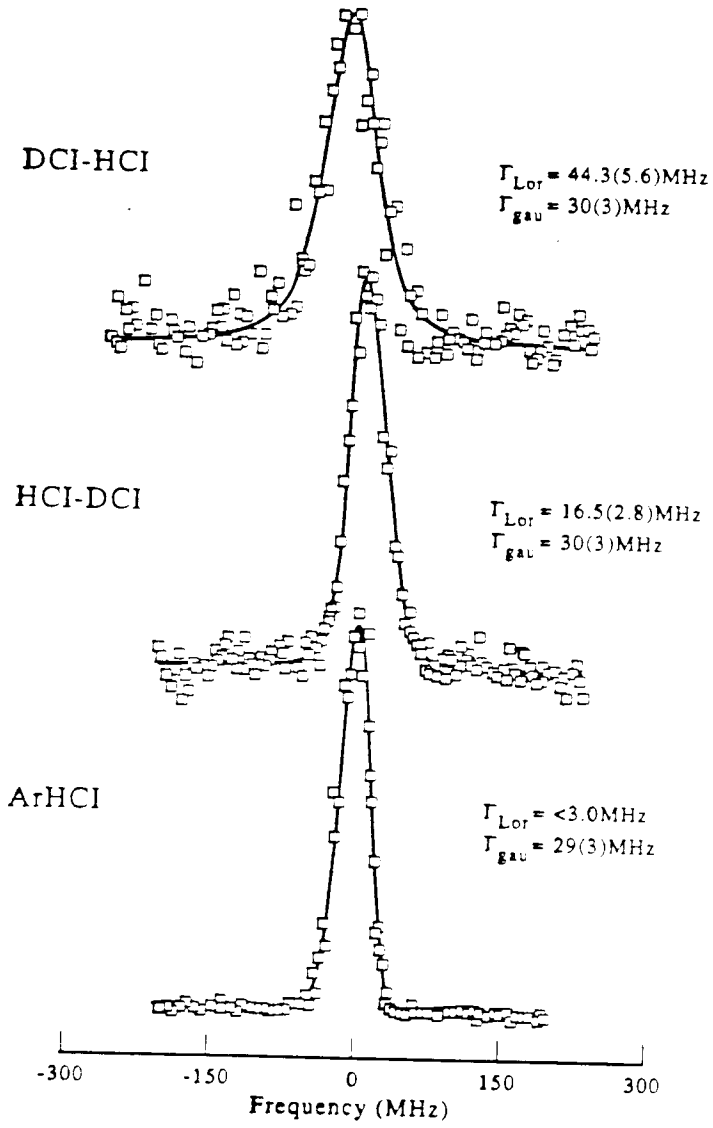

Figure 2.22 A demonstration of predissociation broadening. The lower trace is due to ArHCl which is expected to have a very long vibrationally excited lifetime (ie. determined to be >0.3 ms, which would correspond to a Lorentzian width of 500 Hz). The middle trace is due to HCl vibrational excitation of HCl-DCl. This line shape is broader than that of ArHCl but narrower than that HCl excitation of DCl-HCl. As will be discussed in Chapter VI, this is due to a significantly shorter lifetime for DCl-HCl than HCl-DCl.

References for Chapter II

1. M.D. Schuder, D.D. Nelson Jr., D.J. Nesbitt, J. Chem. Phys. **94**, 5796 (1991).

2. M.D. Schuder, C.M. Lovejoy, D.D. Nelson Jr., and D.J. Nesbitt, J. Chem. Phys. **91**, 4418 (1989).

3. M.D. Schuder, D.D. Nelson Jr., and D.J. Nesbitt, (in preparation).

4. M.D. Schuder and D.J. Nesbitt (in preparation).

5. M.D. Schuder, C.M. Lovejoy, R. Lascola, and D.J. Nesbitt (in preparation).

6. C.M. Lovejoy and D.J. Nesbitt, J. Chem. Phys. **86**, 3151 (1987).

7. C.M. Lovejoy, PhD. Thesis, University of Colorado (1990).

8. A. McIlroy, Ph.D. Thesis, University of Colorado (1991).

9. G.P. Agrawal and H.K. Dutta, Long-Wavelength Semiconductor Lasers (Van Nostrand-Reinhold, New York, 1986).

10. N. Hunt, S.C. Foster, J.W.C. Johns, and A.R.W. McKellar, J. Mol. Spec. **111**, 42 (1985).

11. A.S. Pine, J. Opt. Soc. Am. **64**, 1683 (1974).

12. J.U. White, J. Opt. Soc. Am. **32**, 285 (1942).

13. J.L. Hall and S.A. Lee, Appl. Phys. Lett. **29**, 367 (1976).

14. G. Guelachvili, Opt. Comm. **19**, 150 (1976).

15. C.M. Lovejoy and D.J. Nesbitt, Rev. Sci. Instrum. **58**, 807 (1987).